Application of a Cosserat Continuum Model to Non-associated Plasticity

Sepideh Alizadeh Sabet

Department of Civil and Structural Engineering
University of Sheffield

A thesis submitted in partial fulfilment for the degree of Doctor of Philosophy

January 2020

Application of a Cosserat Continuum Model to Non-associated Plasticity

Sepideh Alizadeh Sabet

Department of Civil and Structural Engineering
University of Sheffield

A thesis submitted in partial fulfilment for the degree of Doctor of Philosophy

January 2020

Declaration

I, Sepideh Alizadeh Sabet, ensure this PhD thesis is independently written and no sources have been used other than the stated references.

Sepideh Alizadeh Sabet
January 2020

Abstract

A severe, spurious dependence of numerical simulations on the mesh size and orientation can be observed in elasto-plastic models with a non-associated flow rule. Such mesh dependency effects are quite well-known and vastly investigated in problems with the presence of strain softening in the constitutive relation. However, other material instabilities, like non-associated plastic flow, can also cause mesh sensitivity. Indeed, loss of well-posedness of the problem in quasi-static analyses is the fundamental cause of the observed mesh dependence. It has been known since long that non-associated plastic flow can cause loss of stability, but the consequence for mesh sensitivity, and subsequently, for the difficulty of the equilibrium-finding iterative procedure to converge, have remained largely unnoticed. The present thesis deals with exploring the possibility of using non-standard continua, namely the Cosserat continuum models, in non-associated plasticity problems to tackle the pathological mesh dependencies not only on the size of the elements but also on the orientation of them. The motivation in this thesis for using the Cosserat continuum models for this purpose, lies in the additional parameters that are specified in such a model, i.e. the micro-rotations and characteristic length scale. These features make the Cosserat continuum model a suitable choice to simulate and capture the behavior of the granular and geomaterials. The characteristic length scale helps regularise the strain localisation problems and prevent loss of uniqueness of solution. The mesh size dependency of the results for classical non-associated plasticity models is analysed in depth using an infinitely long shear layer. It is shown that the mesh effect disappears when the standard continuum model is replaced by a Cosserat continuum. Next, the dependence of the shear-band inclination in a biaxial test on the mesh size as well as on the mesh orientation is investigated. The orientation of the developed shear band is found to be dependent on the orientation of the mesh for classical models. Using a Cosserat continuum model, numerical solutions result for shear-band formation which are independent of the size and the orientation of the discretisation.[1] , [2]

[1]Partly based on: Sabet, S. A. and de Borst, R. (2019). Structural softening, mesh dependence, and regularisation in non-associated plastic. *International Journal for Numerical and Analytical Methods in Geomechanics*, 43(13):2170-2183

[2]Partly based on: Sabet, S. A. and de Borst, R. (2019). Mesh bias and shear band inclination in standard and non-standard continua. *Archive of Applied Mechanics*, 89(12): 2577-2590.

Acknowledgements

This work has been carried out at the Department of Civil and Structural Engineering of the University of Sheffield. I would like to express my deepest gratitude to my supervisor, Professor René de Borst for believing in me and giving me this exceptional opportunity to undertake my PhD thesis in his research group at the University of Sheffield. I am greatly indebted to him for his advice and encouragements, our many fruitful and stimulating discussions, and his incredibly generous and unstinting support for me during my PhD journey.

I wish to extend my sincere appreciation to Professor Harm Askes for his tremendous support and willingness to help the PhD students during his time as the Head of the Department of Civil and Structural Engineering of the University of Sheffield. Furthermore, I am extremely thankful to him and Dr. Antonis Zervos for accepting to act as examiners of my thesis and their insightful comments and suggestions. Special thanks go to Dr. Erik Jan Lingen at Dynaflow Research Group for his assistance and support regarding the software Jem/Jive.

Last but not least, I would like to thank my wonderful family, mum, dad, Soodabeh and Samira, for always being by my side and caring for me.

The financial support by ERC Advanced Grant 664734 “PoroFrac” for this work is gratefully acknowledged.

Table of contents

List of figures

List of tables

Chapter 1

Introduction [1], [2]

1.1 Motivation

The current thesis has come out of the research on a project in a wider context on implicit finite element analysis of the fault rupture under shear in rocks including the off-fault energy dissipation. Taking the inelastic energy dissipation in the bulk of materials adjacent to the fault is relevant for capturing a more realistic rupture velocity of a fault during an earthquake. The underlying reason is that a damage zone of finite thickness develops in the material bordering the fault due to large concentrated stresses ahead of the rupture front. The importance of taking the inelastic response of the bulk material in addition to the fault itself has been pointed out in [3, 4, 73, 78, 81]. The intended numerical solver for this challenging problem was the implicit time integration, as it is more suitable for earthquake loadings and also ensures the satisfaction of balance of linear momentum.

There have been some attempts in the literature to address this problem. A similar work has been done using finite difference method [4]. In [99], a Drucker-Prager plasticity model for the off-fault bulk material has been assumed and an explicit commercial FEA solver ABAQUS has been used. In an extension to this work, the effect of fluid in the material has been included [110]. In [112], an isogeometric model has been developed for a fluid-saturated porous medium which captures the fracture at the faults and the fluid pressure changes at the cavities. However, the energy dissipation off the slip zone is not taken into account.

In the author's initial investigations, a model was implemented and set up under 2D plane strain condition as can be seen in Figure 1.1. The fault is modelled as a notch in

[1] Partly based on: Sabet, S. A. and de Borst, R. (2019). Structural softening, mesh dependence, and regularisation in non-associated plastic. *International Journal for Numerical and Analytical Methods in Geomechanics*, 43(13): 2170-2183

[2] Partly based on: Sabet, S. A. and de Borst, R. (2019). Mesh bias and shear band inclination in standard and non-standard continua. *Archive of Applied Mechanics*, 89(12): 2577-2590.

the middle and cohesive interface elements [92, 111] are inserted along the crack path to allow for crack propagation along the fault. These zero thickness interface elements obey a linear-exponential cohesive traction separation law and were developed and implemented in the software Jive [85]. The off-fault material is modelled by elasto-plastic constitutive law with non-associative flow rule suitable for rocks. The non-associative flow rule is needed for realistic simulation of these materials as an associative flow rule usually overestimates the amount of plastic strains in pressure sensitive materials.

The incremental-iterative solvers in implicit finite element analysis run into severe convergence problems for the above described numerical model up to a point that they fail and no convergence can be achieved. Further investigations were carried out to pin point the source of the convergence problem. It turned out to be the use of non-associated flow rule in the plasticity model which leads to the ill-posedness of the boundary value problem and can cause both mesh-size and mesh-orientation dependency of the results as well as convergence issues for the solvers. This will be explained in more detail in chapter 2. Therefore, in order to continue with the original research problem, the author realised the need to first address the convergence and mesh dependence problems for non-associated plasticity. Hence, following this chapter, this thesis will focus on tackling non-associated plasticity problems.

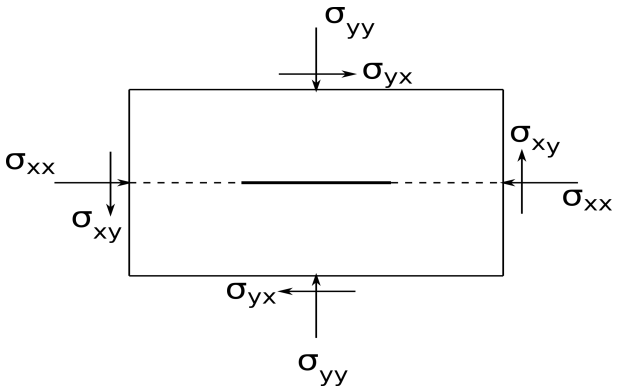

Fig. 1.1 Model for numerical investigations of fault rupture in 2D plane strain conditions

1.2 Scope of the thesis

The main goal of this thesis is to develop an efficient numerical model to simulate the behaviour of pressure sensitive elasto-plastic materials with non-associative flow rule, e.g. rocks, when they go through localisation. The numerical results should be mesh-objective, both in terms of size and orientation and the convergence behaviour of the incremental-iterative solvers should be improved as well.

Various approaches have been proposed to regularise the problem of strain localisation. Non-local models [9, 10, 72] or gradient continua [29, 62, 71, 82, 101, 116] are regularisation methods which can avoid local loss of well-posedness. Inclusion of viscosity and rate effects have also been proven effective in regularising the boundary-value problem [31, 51, 66]. The approach adopted in the scope of this thesis, is to use Cosserat continuum models [19]. The Cosserat continuum model is particularly applicable to granular materials as it is capable of taking the microstructure of the material into account via micro-rotations, representing the average spin of the particles, as an additional degree of freedom [97]. It has subsequently been used to regularise constitutive models of granular materials and rocks [25, 26, 30, 61, 63, 70]. Papanastasiou and Zervos have shown in [69], that both Cosserat and Gradient elasto-plasticity could be used to regularise the ill-posed problem of strain softening. Cosserat model has been applied successfully by Zervos to capture the grain rotations which influence the initial localisation in sandstone material for the problem of stability of underground openings [117]. Cosserat continuum models have been used previously to tackle the mesh size dependence in localisation problems due to explicit softening in the constitutive models. The novelty of the current thesis lies in the application of a Cosserat elasto-plasticity model to regularise the plasticity problems with non-associated flow in the absence of any explicit softening. To focus on non-associated flow as the sole destabilising effect, strain softening and possible geometrical destabilising effects have been excluded from the analyses in this thesis.

1.3 Objectives

In order to achieve the main goal of this thesis, the following objectives are fulfilled:

- Investigation of loss of uniqueness of solution leading to ill-posedness in non-associated plasticity problems under quasi-static loading conditions.
- Implementation of reliable numerical algorithms for classical non-associated plasticity models which also include special treatment of singularities of the yield surface.
- Development and numerical implementation of a Cosserat non-associated plasticity model.
- Investigation of the performance of the classical non-associated plasticity models in localisation problems.

- Investigation of the performance of the Cosserat plasticity model in terms of mesh size and orientation dependency and convergence behaviour of the numerical solver at hand of a 1D shear layer and a 2D biaxial test.

1.4 Software used

All the numerical models and formulations in this thesis have been implemented in the software Jem/Jive [39]. It is a research-oriented C++ software development kit developed by the DynaFlow research Group and can be used for numerical simulations. Matlab [55] and ParaView [1] have been used for post-processing purposes throughout this work.

1.5 Structural outline

Following this introductory chapter, the rest of thesis is organized as follows:

- Two classical non-associated plasticity models, namely the Mohr-Coulomb and Drucker-Prager models, are reviewed in **chapter 2**. The governing equations are shown and numerical implementation of these models is discussed. Special care is taken in these algorithms to treat the singularities in the yield surfaces of these models. Next, a background to pathological mesh dependency in numerical simulations is given at hand of a simple example. The underlying mathematical condition which causes loss of uniqueness of the solution is then discussed for a Mohr-Coulomb plasticity model with a non-associated flow embedded in a standard continuum.

- In **chapter 3**, the concept and governing equations of a Cosserat continuum model are reviewed. The numerical implementation for a 2D Cosserat continuum model is also presented.

- In **chapter 4**, the application of Cosserat continuum models to remove mesh dependency is investigated. For this purpose, a 1D infinite layer under shear and a 2D biaxial compression test are considered to investigate the efficiency of Cosserat continuum models to remove both the mesh size and orientation dependencies.

- Finally, major outcomes of this thesis are summarized and suggestions on possible future work as the continuation of this thesis, are made in **chapter 5**.

Chapter 2

Classical cohesive-frictional plasticity models

2.1 Introduction

Most of the geomaterials like soils and rock masses are porous and thus the pressure of the fluid trapped in the pores of them can influence their strength. Moreover, materials like soils and rock masses show a pressure dependent cohesive-frictional constitutive behaviour. Such behaviour can be captured with the classical Mohr-Coulomb or Drucker-Prager plasticity models [21, 35]. In both criteria, the failure is determined by the maximum shear stress which depends on the normal stress. In case of zero friction, the Mohr-Coulomb and the Drucker-Prager models become equivalent to Tresca and Von Mises models, respectively . Hence they can be regarded as an extension of Tresca and Von Mises plasticity models for pressure sensitive materials.

In this chapter, the governing equations for a general elasto-plastic constitutive model are first briefly presented. The reader is referred to [45, 64, 74] for a detailed insight into fundamental elements of plasticity, e.g. yield functions, plastic flow rule, etc. Then the definition of non-associativity and the concept of dilatancy will follow. Next, the Mohr-Coulomb and the Drucker-Prager plasticity models are discussed in details and two verification examples are shown. Then an introductory background to localisation and mesh dependency in numerical simulations is given. Finally, the loss of uniqueness of solution in classical non-associated plasticity problems is discussed at the end of this chapter.

2.2 Governing equations for a general rate-independent elasto-plastic constitutive model

Under small strain theory, the strain tensor ($\boldsymbol{\varepsilon}$) can be additively decomposed into elastic ($\boldsymbol{\varepsilon}^e$) and plastic parts ($\boldsymbol{\varepsilon}^p$)

$$\boldsymbol{\varepsilon} = \boldsymbol{\varepsilon}^e + \boldsymbol{\varepsilon}^p \tag{2.1}$$

The corresponding rate form reads

$$\dot{\boldsymbol{\varepsilon}} = \dot{\boldsymbol{\varepsilon}}^e + \dot{\boldsymbol{\varepsilon}}^p \tag{2.2}$$

Assuming linear isotropic elasticity and no hardening, the free energy storage in this model $\Psi(\boldsymbol{\varepsilon}^e)$ takes the form

$$\Psi(\boldsymbol{\varepsilon}^e) = \frac{1}{2}\kappa(\mathrm{tr}\boldsymbol{\varepsilon}^e)^2 + \mu\ \mathrm{dev}\boldsymbol{\varepsilon}^e : \mathrm{dev}\boldsymbol{\varepsilon}^e \tag{2.3}$$

where κ and μ are the bulk and shear moduli, respectively. Between the stress and elastic strain rates, a bijective relationship hold:

$$\dot{\boldsymbol{\sigma}} = \mathbf{D}^e : (\dot{\boldsymbol{\varepsilon}} - \dot{\boldsymbol{\varepsilon}}^p) \tag{2.4}$$

where $\mathbf{D}^e$ is the elastic stiffness tensor.

In plasticity, a condition defines the start of plastic deformation which is known as the yield criterion. For perfect plasticity it is a function of stresses as $f(\boldsymbol{\sigma})$.The elastic domain,$\mathbb{E}$, is defined by this yield function as:

$$\mathbb{E} = \{\boldsymbol{\sigma} |\ f(\boldsymbol{\sigma}) < 0\} \tag{2.5}$$

Once the stress state reaches the yield surface, the plastic deformations need to be computed. The evolution of plastic strains is governed by the following formula known as the flow rule [45, 57, 59]

$$\dot{\boldsymbol{\varepsilon}}^p = \dot{\gamma}\frac{\partial g}{\partial \boldsymbol{\sigma}} \tag{2.6}$$

Here g is known as the plastic potential, γ is the plastic multiplier and $\dot{\gamma}$ is the rate of it.

A constraint known as the consistency condition ensures that once the material yields, the stress state remains on the yield surface for a short amount of time:

$$\dot{f} = 0 \tag{2.7}$$

The plastic multiplier can be determined from the consistency condition as follows:

$$\dot{\gamma} = \frac{f_{\boldsymbol{\sigma}} : \mathbf{D}^e : \dot{\boldsymbol{\varepsilon}}}{f_{\boldsymbol{\sigma}} : \mathbf{D}^e : g_{\boldsymbol{\sigma}}} \tag{2.8}$$

In the above equation, $f_{\boldsymbol{\sigma}}$ and $g_{\boldsymbol{\sigma}}$ denote the derivatives of the yield and plastic potential functions with respect to the stress, respectively.

With the Karush-Kuhn-Tucker (KKT) loading/unloading conditions to ensure the constraint $f \geq 0$ for the plastic deformation to occur, the formalities are complete.

$$\dot{\gamma} \geq 0 \quad , f \leq 0 \quad , \dot{\gamma} f = 0 \tag{2.9}$$

The governing equations for a general perfect plasticity model are summarised in Figure 2.1.

1. kinematics: $\boldsymbol{\varepsilon} = \boldsymbol{\varepsilon}^e + \boldsymbol{\varepsilon}^p$
2. Free energy function: $\Psi(\boldsymbol{\varepsilon}^e) = \frac{1}{2}\kappa(\mathrm{tr}\boldsymbol{\varepsilon}^e)^2 + \mu\, \mathrm{dev}\boldsymbol{\varepsilon}^e : \mathrm{dev}\boldsymbol{\varepsilon}^e$
3. Stress: $\dot{\boldsymbol{\sigma}} = \mathbf{D}^e : (\dot{\boldsymbol{\varepsilon}} - \dot{\boldsymbol{\varepsilon}}^p)$
4. Yield function: $f(\boldsymbol{\sigma})$
5. Plastic potential: $g(\boldsymbol{\sigma})$
6. Consistency condition: $\dot{f} = 0$
7. Flow rule: $\dot{\boldsymbol{\varepsilon}}^p = \dot{\gamma}\frac{\partial g}{\partial \boldsymbol{\sigma}}$
8. Rate of plastic multiplier: $\dot{\gamma} = \frac{f_{\boldsymbol{\sigma}} : \mathbf{D}^e : \dot{\boldsymbol{\varepsilon}}}{f_{\boldsymbol{\sigma}} : \mathbf{D}^e : g_{\boldsymbol{\sigma}}}$
9. KKT loading/unloading conditions: $\dot{\gamma} \geq 0 \quad , f \leq 0 \quad , \dot{\gamma} f = 0$

Fig. 2.1 Governing equations for a general perfect plasticity model

2.3 Return mapping algorithm for rate-independent perfect-plasticity

The numerical integration of rate equations summarised in the previous section, can be done with a return mapping scheme. A strain-driven process is considered. The values of the quantities at the previous and current time steps are denoted by $(.)_n$ and $(.)_{n+1}$, respectively. Given the state $(\boldsymbol{\varepsilon}_n, \boldsymbol{\varepsilon}_n^p)$ and the strain increment $\Delta\boldsymbol{\varepsilon}$, the values for stress and state variables are computed at the end of the load step.

The return mapping used here consists of two steps, an elastic predictor step and a plastic corrector step. At each time step t_{n+1}, the step is assumed to be fully elastic and no plastic deformation occurs. A trial stress state $\boldsymbol{\sigma}_{n+1}^{\text{trial}}$ is then computed as:

$$\boldsymbol{\sigma}_{n+1}^{\text{trial}} = \boldsymbol{\sigma}_{n+1} + \mathbf{D}^e \Delta\varepsilon \tag{2.10}$$

This trial stress is plugged into the yield function equation which leads to a trial value for the yield criterion f^{trial}. Now if the value of f^{trial} is negative, then the assumption of elastic state was correct and all the variables have been computed correctly, otherwise a plastic corrector step is needed to return the stress state on the yield surface. For this purpose, first the incremental plastic multiplier should be computed. For the integration of rate of plastic multiplier a backward Euler method is used. The choice of an implicit scheme over an explicit scheme relates to stability and accuracy. The implicit integration methods are more accuaret than the explicit methods as the solution might drift away from the yield surface using the latter[36] . While with advanced explicit algorithms, the accuracy can be improved [95], the stability requirement is often not met. This holds in particular when the yield surface is locally strongly curved, where explicit algorithms can become poor, with implicit algorithms in principle remaining unconditionally stable [67]. A corner, as in Mohr-Coulomb is an extreme form, with a zero radius of curvature. Therefore, an implicit integration method is a safer method to adopt. A backward Euler integration of the Eq. (2.8) leads to:

$$\Delta\gamma = \frac{f_{\boldsymbol{\sigma}}|_{n+1} : \mathbf{D}^e : \Delta\boldsymbol{\varepsilon}_{n+1}}{f_{\boldsymbol{\sigma}}|_{n+1} : \mathbf{D}^e : g_{\boldsymbol{\sigma}}|_{n+1}} \tag{2.11}$$

With the value of incremental plastic multiplier at hand, the incremental plastic strains can be integrated in the same way by backward Euler integration from Eq. (2.6)

$$\Delta\boldsymbol{\varepsilon}^p = \Delta\gamma \frac{\partial g}{\partial \boldsymbol{\sigma}}\Big|_{n+1} \tag{2.12}$$

The plastic strains can now be updated as:

$$\boldsymbol{\varepsilon}_{n+1}^p = \boldsymbol{\varepsilon}_n^p + \Delta\boldsymbol{\varepsilon}^p \tag{2.13}$$

The incremental stresses can be integrated from Eq. (2.4)

$$\Delta\boldsymbol{\sigma} = \mathbf{D}^e : (\Delta\boldsymbol{\varepsilon}_{n+1} - \Delta\boldsymbol{\varepsilon}_{n+1}^p) \tag{2.14}$$

By definition the updated stress is:

$$\boldsymbol{\sigma}_{n+1} = \boldsymbol{\sigma}_n + \Delta\boldsymbol{\sigma} \tag{2.15}$$

Substitution of Eq. (2.4) into Eq. (2.15) leads to the value for updated stresses:

$$\boldsymbol{\sigma}_{n+1} = \boldsymbol{\sigma}^{\text{trial}}_{n+1} - \mathbf{D}^e \Delta\boldsymbol{\varepsilon}^p_{n+1} \tag{2.16}$$

2.4 Definition of non-associativity of the plastic flow

In associated plasticity models, the plastic flow potential g, is the same as the yield function f:

$$g = f \tag{2.17}$$

Otherwise, the model is said to be non-associated.

2.5 Dilatancy

In 1885, Reynolds reported about the dilatancy in granular materials [77] . It is referred to the change in volume of an element in the material under shear. In 1985, the dilation angle was introduced [42] and controls the plastic volumetric strain of the material over the plastic shear strain and here is denoted by ψ. The concept of dilation and dilation angle can be visualised in Figure 2.2, where the material is represented by a pack of incompressible spheres. Dilation angle can be positive or negative. The former is the case for example for dense sand as the total volume of the material increases by particles moving on each other under shear. For loose sand the dilation angle is negative and the total volume of the material decreases under shear.

The need for incorporating a non-associated flow rule arises from the overestimation of the volumetric plastic strains computed with the associated models when compared to experiments. Therefore, a non-associated flow rule results in more accurate displacements.

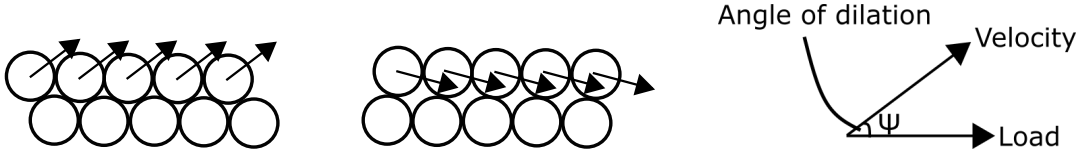

(a) Dilating materials (b) Compacting materials (c) Dilation angle

Fig. 2.2 Ball analogy: Concept of dilation

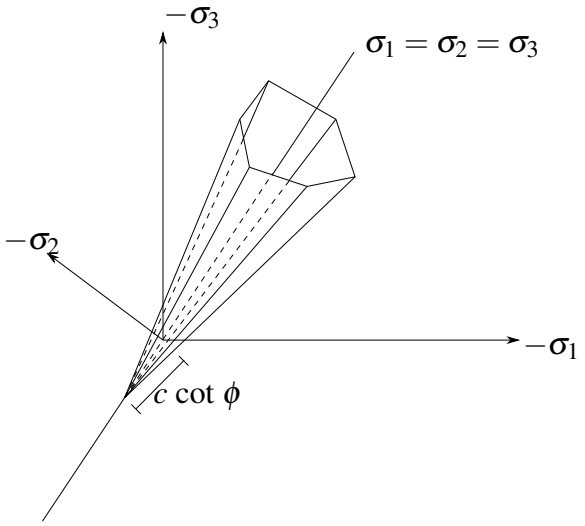

Fig. 2.3 Mohr-Coulomb Plasticity yield function in principal stress space

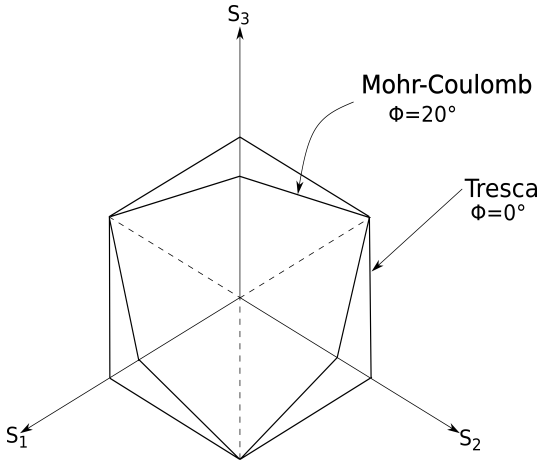

Fig. 2.4 Mohr-Coulomb Plasticity yield function on deviatoric or π plane

2.6 Mohr-Coulomb plasticity model

Mohr-Coulomb plasticity model defines the yield surface with a relationship between the normal and shear stresses as in Eq. (2.18)

$$\tau = c - \sigma_n \tan\phi \tag{2.18}$$

where σ_n is the normal stress which is assumed tensile positive. c is the cohesion constant. When normal stress is zero, the strength is positive if $c > 0$ and zero if $c = 0$. ϕ is the angle of internal friction indicating how pressure dependent the strength of the material is.

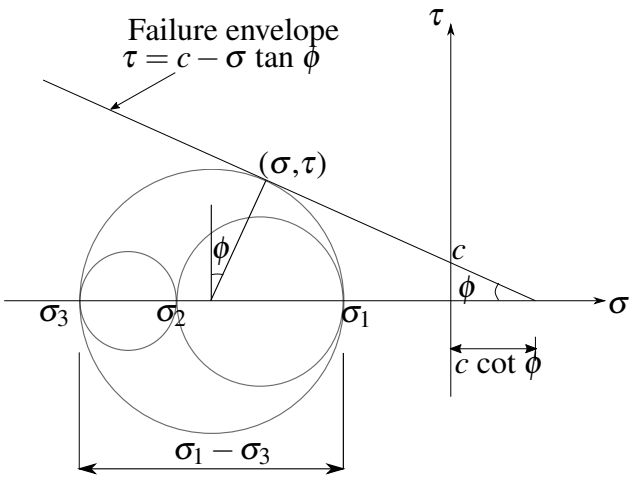

Fig. 2.5 Mohr circle

Eq. (2.18) can be recast in terms of the principal stresses as follows:

$$\frac{\sigma_1 - \sigma_3}{2}\cos\phi = c - (\frac{\sigma_1 + \sigma_3}{2} + \frac{\sigma_1 - \sigma_3}{2}\sin\phi)\tan\phi \tag{2.19}$$

which can be rearranged as:

$$(\sigma_1 - \sigma_3) + (\sigma_1 + \sigma_3)\sin\phi = 2c\cos\phi \tag{2.20}$$

The yield function thus reads as:

$$f(\boldsymbol{\sigma}, c) = (\sigma_1 - \sigma_3) + (\sigma_1 + \sigma_3)\sin\phi - 2c\cos\phi \tag{2.21}$$

The above yield surface is an irregular hexagon in the principal stress space along the hydrostatic axis (where all the principapal stresses are equal as $\sigma_1 = \sigma_2 = \sigma_3$) and in π-plane, as visualised in Figures 2.3 and 2.4. In Figure 2.5, the stress state at yield is shown by the Mohr circles' positions to the failure line defined by Eq. (2.18). The apex of the Mohr-Coulomb yield surface is located at $p_{\text{apex}} = c\cot\phi$ on the hydrostatic axis and controls the maximum tensile strength of the material.

For a non-associated Mohr-Coulomb plasticity model, a plastic potential similar in form to the yield function can be considered:

$$g(\boldsymbol{\sigma}) = (\sigma_1 - \sigma_3) + (\sigma_1 + \sigma_3)\sin\psi \tag{2.22}$$

2.6.1 The influence of the out-of-plane stress σ_z in plane strain problems

In Mohr-Coulomb model, the intermediate principal stress does not play a role in defining the yield of the material. This might wrongly lead to the assumption that in plane strain problems, the out-of-plane stress is always the intermediate stress and can be excluded in the analysis. However, it has been shown in the literature that the out-of-plane stress is not necessarily always the intermediate principal stress.

In [16], a study has been done on the bearing capacity problem, see Figure 2.6a, for two values of the Poisson's ratio, $\nu = 0.05$ and $\nu = 0.45$. For each value of the Poisson's ratio, two cases have been considered: one including(in total 4 components of the stress tensor) and the other one excluding the σ_z (in total 3 components of the stress tensor), keeping all other parameters the same. This study shows that for low values of the Poisson's ratio, there is a slight difference, between the results of simulations with and without including σ_z as is illustrated in Figure 2.6b. Although the slightly different results could have also possibly emerged from numerical errors in the computations, a more conservative approach would be to include the out-of-plane stress in the computations as well. Another example is given in [18] considering the cases where the principal elastic in-plane strains are equal which leads to the σ_z being equal to the maximum or minimum principal stress. It causes the stress state fall on the singularities of the Mohr-Coulomb pyramid. In the same work, a further example of a single element going through a sequence of loadings (Figure 2.7) is given, such that σ_z becomes the maximum principal stress at some point during loading and remains the intermediate principal stress in the beginning of loading and after yielding as is illustrated in Figure 2.8. The loading sequence is as follows: At state 1, $\Delta\sigma_x = -200$ KPa is applied and the material reaches state 2. From state 1 to 2, $\sigma_z = \sigma_2$. Then at state 2, $\Delta\varepsilon_y = -1 \times 10^{-3}$ is applied while keeping σ_x constant. In the transition between state 1 and 2, there are 3 stages: Stage 1 is when the σ_z is not the intermediate principal stress anymore but is the major principal stress and σ_y is the intermediate principal stress, such that $\sigma_z \geq \sigma_y \geq \sigma_x$. Then the material reaches stage 2, where the σ_z is still the major principal stress but σ_x is the intermediate principal stress, such that $\sigma_z \geq \sigma_x \geq \sigma_y$. At stage 3, the σ_z becomes the intermediate principal stress again and the material yields. After this point we have $\sigma_x \geq \sigma_z \geq \sigma_y$. The material parameters used for this simulation are given in table 2.1. The above examples show the importance of including the out-of-plane stress in the elasto-plastic calculations using Mohr-Coulomb model and this is also taken into account in the remainder of this thesis.

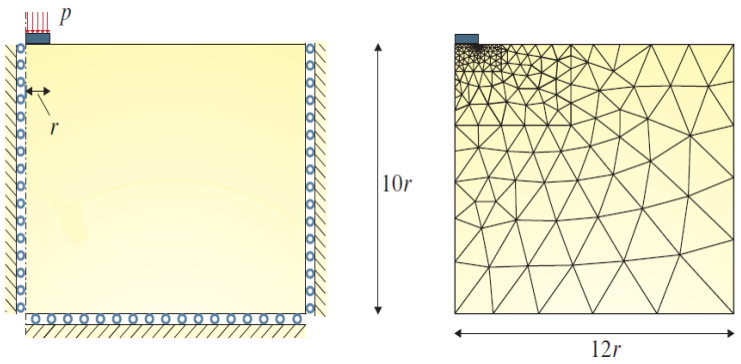

(a) Model geometry and boundary conditions and the mesh

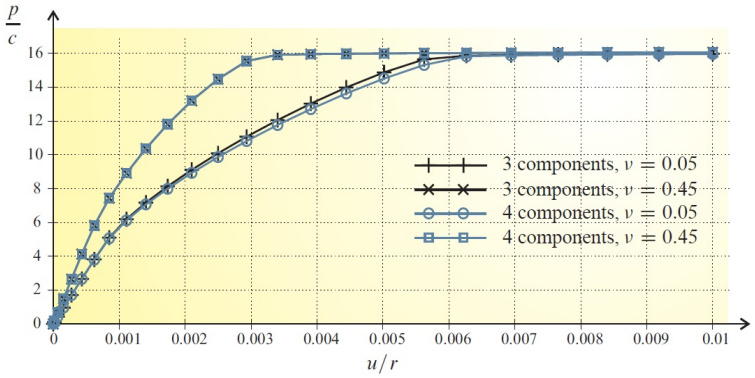

(b) Normalised pressure vs settlement

Fig. 2.6 Bearing problem for two cases with three and four component stress vector, taken from [16]

2.6.2 Numerical implementation

Here the formulations and the algorithm developed in [32] are adopted for the implementation of the non-associated Mohr-Coulomb model. The stress update procedure is carried out in the principal stress space. The yield surface of the Mohr–Coulomb hexagon in the principal stress space can also be cast into six yield functions on each face:

$$f_1(\boldsymbol{\sigma},c) = (\sigma_1-\sigma_3)+(\sigma_1+\sigma_3)\sin\phi - 2c\cos\phi \tag{2.23}$$
$$f_2(\boldsymbol{\sigma},c) = (\sigma_2-\sigma_3)+(\sigma_2+\sigma_3)\sin\phi - 2c\cos\phi \tag{2.24}$$
$$f_3(\boldsymbol{\sigma},c) = (\sigma_2-\sigma_1)+(\sigma_2+\sigma_1)\sin\phi - 2c\cos\phi \tag{2.25}$$
$$f_4(\boldsymbol{\sigma},c) = (\sigma_3-\sigma_1)+(\sigma_3+\sigma_1)\sin\phi - 2c\cos\phi \tag{2.26}$$
$$f_5(\boldsymbol{\sigma},c) = (\sigma_3-\sigma_2)+(\sigma_3+\sigma_2)\sin\phi - 2c\cos\phi \tag{2.27}$$
$$f_6(\boldsymbol{\sigma},c) = (\sigma_1-\sigma_2)+(\sigma_1+\sigma_2)\sin\phi - 2c\cos\phi \tag{2.28}$$

Table 2.1 Parameters used for the Mohr-Coulomb model in Figure 2.7

Parameter	Symbol	Value
Young's modulus	E	100 MPa
Poisson's ratio	ν	0.3
Internal friction angle	ϕ	20^o
Dilation angle	ψ	20^o
Cohesion	c	100 KPa

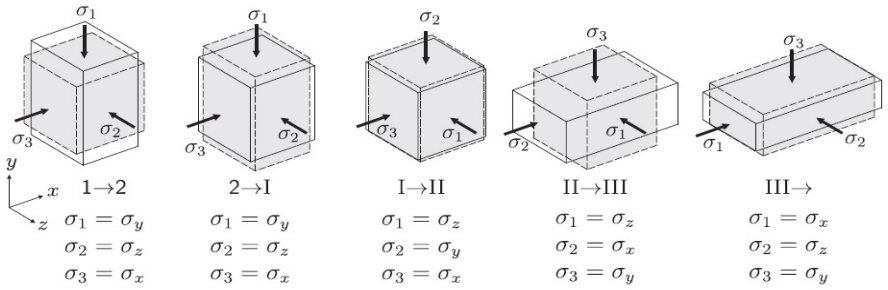

Fig. 2.7 Material point going through a set of loadings in x and y directions, taken from [18]

where each $f_i(\boldsymbol{\sigma}, c) = 0$, defines one face of the Mohr–Coulomb pyramid.
The plastic potential functions (g_i) are also considered in the same way:

$$g_1(\boldsymbol{\sigma}, c) = (\sigma_1 - \sigma_3) + (\sigma_1 + \sigma_3)\sin\psi \tag{2.29}$$

$$g_2(\boldsymbol{\sigma}, c) = (\sigma_2 - \sigma_3) + (\sigma_2 + \sigma_3)\sin\psi \tag{2.30}$$

$$g_3(\boldsymbol{\sigma}, c) = (\sigma_2 - \sigma_1) + (\sigma_2 + \sigma_1)\sin\psi \tag{2.31}$$

$$g_4(\boldsymbol{\sigma}, c) = (\sigma_3 - \sigma_1) + (\sigma_3 + \sigma_1)\sin\psi \tag{2.32}$$

$$g_5(\boldsymbol{\sigma}, c) = (\sigma_3 - \sigma_2) + (\sigma_3 + \sigma_2)\sin\psi \tag{2.33}$$

$$g_6(\boldsymbol{\sigma}, c) = (\sigma_1 - \sigma_2) + (\sigma_1 + \sigma_2)\sin\psi \tag{2.34}$$

The plastic flow vector ($\mathbf{N}$) is then computed for each sextant of the Mohr-Coulomb pyramid as:

$$\mathbf{N}^i = \frac{\partial g_i}{\partial \boldsymbol{\sigma}} \tag{2.35}$$

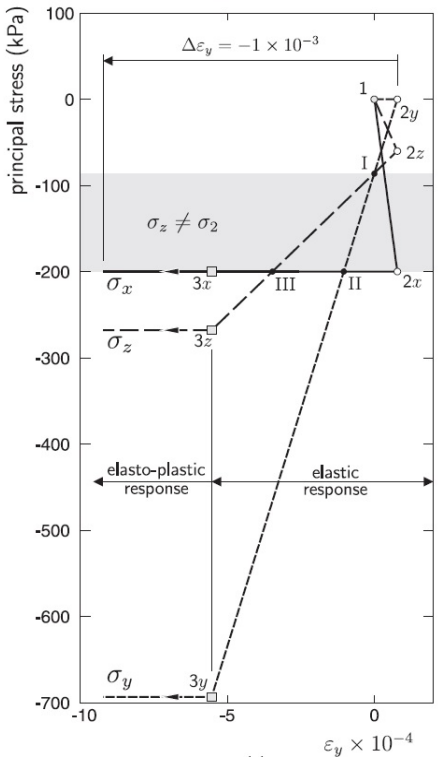

Fig. 2.8 Principal stress-strain states, taken from [18]

Koiter's Generalisation

Mohr-Coulomb yield surface is not continously differentiable and has singularities at the apex and at the edges where two planes meet. At these singularities, there is a need for a special numerical treatment when computing the flow vector. According to [47] the plastic flow vector can be computed as a linear combination of all the flow vectors adjacent to that singularity as

$$\dot{\boldsymbol{\varepsilon}}^p = \sum_{i=1}^{n} \dot{\gamma}_i \mathbf{N}^i \tag{2.36}$$

where:

$$\dot{\gamma}_i \geq 0 \qquad i = 1, ..., n \tag{2.37}$$

The Koiter's generalisation is visualized in Figure 2.9.

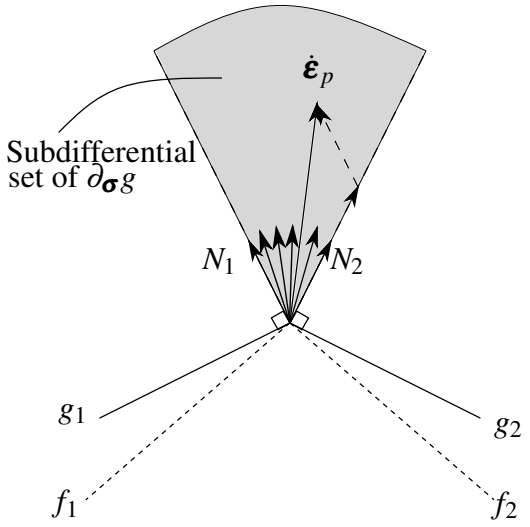

Fig. 2.9 Plastic flow direction according to Koiter's generalisation

Stress update procedure

The stress update algorithm uses a return mapping scheme which was explained in section 2.3. The trial elastic strains and stresses are computed as follows:

$$\boldsymbol{\varepsilon}_{n+1}^{e,\text{trial}} := \boldsymbol{\varepsilon}_n^e + \Delta\boldsymbol{\varepsilon} \tag{2.38}$$

$$\boldsymbol{\sigma}_{n+1}^{\text{trial}} := 2\mu\,\text{dev}(\boldsymbol{\varepsilon}_{n+1}^{e,\text{trial}}) + \kappa\,\text{tr}(\boldsymbol{\varepsilon}_{\text{n+1}}^{\text{e,trial}})\mathbf{I} \tag{2.39}$$

Then the trial stresses are decomposed into the principal components and ordered as $\sigma_1^{\text{trial}} \geq \sigma_2^{\text{trial}} \geq \sigma_3^{\text{trial}}$. This has the advantage that simplifies the analysis to a single sextant of the Mohr–Coulomb pyramid.
Next the trial value of the yield function is computed to determine if the step is plastic:

$$f^{\text{trial}} = \sigma_1^{\text{trial}} - \sigma_3^{\text{trial}} + (\sigma_1^{\text{trial}} + \sigma_3^{\text{trial}})\sin\phi - 2c\cos\phi \tag{2.40}$$

If $f^{\text{trial}} < 0$, then the step is elastic and there is no need to do the plastic correction step. All variables take their trial values:

$$(.)_{n+1} := (.)_{n+1}^{\text{trial}} \tag{2.41}$$

If $f^{\text{trial}} \geq 0$, then a general return mapping is done. Accounting for the flow rule by Koiter's generalisation in Eq. (2.16), the updated stresses are:

$$\boldsymbol{\sigma}_{n+1} = \boldsymbol{\sigma}_{n+1}^{\text{trial}} - \mathbf{D}^e : \sum_{i=1}^{6} \Delta\gamma^i \mathbf{N}_{n+1}^i \tag{2.42}$$

Eq. (2.42) can be recast in principal stresses as

$$\sigma_j = \sigma_j^{\text{trial}} - \sum_{i=1}^{6} \Delta\gamma^i (2\mu [\mathbf{N}_d^i]_j + \kappa N_v^i); \qquad j = 1,2,3 \tag{2.43}$$

where:
$\mathbf{N}^i$ is the flow vector at the updated stress state
$N_v^i := \text{tr}[\mathbf{N}^i]$ is the volumetric part of $\mathbf{N}^i$
$[\mathbf{N}_d^i]_j$ is the j-th eigenvalue of the deviatoric part of $\mathbf{N}^i$
The backward Euler return mapping takes four forms depending on the location of the trial stresses:

1. **Return to the main plane/smooth portion**:
   In this case only one multiplier is non-zero and the plastic flow vector reads as

$$\mathbf{N}^a := \mathbf{N}^1 = (1+\sin\psi)\mathbf{e}_1 \otimes \mathbf{e}_1 - (1-\sin\psi)\mathbf{e}_3 \otimes \mathbf{e}_3 \tag{2.44}$$

$$\dot{\boldsymbol{\varepsilon}}^p = \dot{\gamma}\mathbf{N}^a \tag{2.45}$$

   Substituting the plastic flow formulation in Eq. (2.43) yields to:

$$\sigma_1 = \sigma_1^{\text{trial}} - \Delta\gamma(2\mu(1+\frac{1}{3}\sin\psi) + 2\kappa\sin\psi) \tag{2.46}$$

$$\sigma_2 = \sigma_2^{\text{trial}} + \Delta\gamma(\frac{4}{3}\mu - 2\kappa)\sin\psi \tag{2.47}$$

$$\sigma_3 = \sigma_3^{\text{trial}} + \Delta\gamma(2\mu(1-\frac{1}{3}\sin\psi) - 2\kappa\sin\psi) \tag{2.48}$$

$$\tag{2.49}$$

   From the consistency condition we compute the incremental plastic multiplier $\Delta\gamma$

$$f = \sigma_1^{\text{trial}} - \sigma_3^{\text{trial}} + (\sigma_1^{\text{trial}} + \sigma_3^{\text{trial}})\sin\phi - 2c\cos\phi - a\Delta\gamma = 0 \tag{2.50}$$

   where

$$a = 4\mu(1+\frac{1}{3}\sin\phi\sin\psi) + 4\kappa\sin\phi\sin\psi \tag{2.51}$$

2. **Return to an edge**:
   Only two plastic multipliers are non-zero

$$\dot{\boldsymbol{\varepsilon}}^p = \dot{\gamma}_a \mathbf{N}^a + \dot{\gamma}_b \mathbf{N}^b \tag{2.52}$$

where
$\mathbf{N}^a$ is the flow vector to the main plane
$\mathbf{N}^b$ is the flow vector to the edge
Whether the return should be made to the right or left edge, is based on geometrical arguments. The corresponding deviatoric parts of the principal stresses at any edge of the Mohr– Coulomb pyramid are equal

$$s_i = s_j \tag{2.53}$$

for s_i, s_j with $i \neq j$
which means at a point on the right edge $s_2 = s_3$ and at a point on the left edge $s_1 = s_2$. The deviatoric decomposition of the stress given by Eq. (2.43) gives:

$$\mathbf{s}_{n+1} = \mathbf{s}^{\text{trial}}_{n+1} - 2\mu(\Delta\gamma^a \mathbf{N}^a_d + \Delta\gamma^b \mathbf{N}^b_d) \tag{2.54}$$

Here $\mathbf{N}^a_d$ and $\mathbf{N}^b_d$ are the deviatoric parts of $\mathbf{N}^a$ and $\mathbf{N}^b$, respectively. $\mathbf{N}^b$ is the normal of the same edge where $\mathbf{s}_{n+1}$ lies. In order to determine whether the $\mathbf{s}^{\text{trial}}_{n+1}$ lies on the left or right edge, a deviatoric tensor $\mathbf{T}$ is used. $\mathbf{T}$ is orthogonal to $\mathbf{N}^a_d$ and has the following eigenvalues :

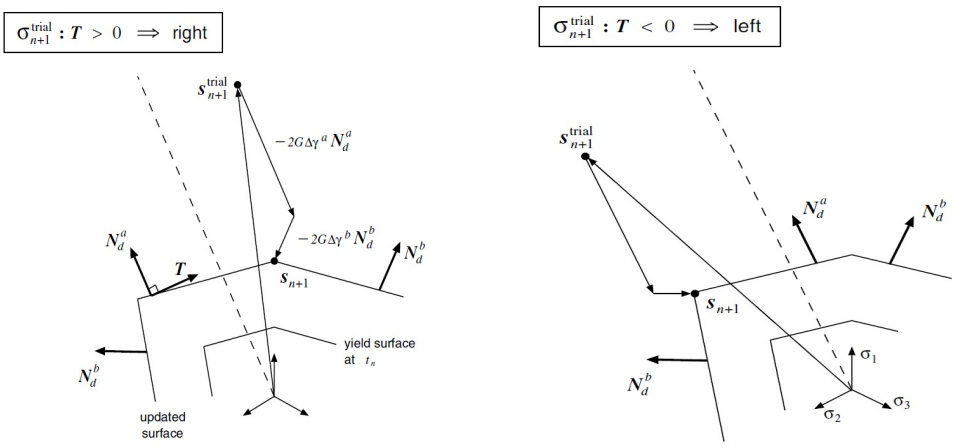

(a) Return to the edge on the right (b) Return to the edge on the left

Fig. 2.10 Selection of the appropriate edge in Mohr-Coulomb model, taken from [32]

$$T_1 = 1 - \sin\psi, T_2 = -2, T_3 = 1 + \sin\psi \tag{2.55}$$

The projection of the $\boldsymbol{\sigma}_{n+1}^{\text{trial}}$ on $\mathbf{T}$ determines to which edge the return should be made. This procedure is visualised in Figure 2.10.

$$S := \mathbf{T} : \boldsymbol{\sigma}_{n+1}^{\text{trial}} = T_1\sigma_1^{\text{trial}} + T_2\sigma_2^{\text{trial}} + T_3\sigma_3^{\text{trial}} \tag{2.56}$$

$$S := (1-\sin\psi)\sigma_1^{\text{trial}} - 2\sigma_2^{\text{trial}} + (1+\sin\psi)\sigma_3^{\text{trial}} \tag{2.57}$$

If $S > 0$, the return should be made to the right edge, otherwise to the left edge.

- **Return to the right edge:**
  At the right edge, $\mathbf{N}^b$ is given as:

$$\mathbf{N}^b := N^6 = (1+\sin\psi)\mathbf{e}_1 \otimes \mathbf{e}_1 - (1-\sin\psi)\mathbf{e}_2 \otimes \mathbf{e}_2 \tag{2.58}$$

  The principal stresses are then updated as follows:

$$\sigma_1 = \sigma_1^{\text{trial}} - (2\mu(1+\frac{1}{3}\sin\psi) + 2\kappa\sin\psi)(\Delta\gamma^a + \Delta\gamma^b) \tag{2.59}$$

$$\sigma_2 = \sigma_2^{\text{trial}} + (\frac{4}{3}\mu - 2\kappa)\sin\psi\Delta\gamma^a + (2\mu(1-\frac{1}{3}\sin\psi) - 2\kappa\sin\psi)\Delta\gamma^b \tag{2.60}$$

$$\sigma_3 = \sigma_3^{\text{trial}} + (2\mu(1-\frac{1}{3}\sin\psi) - 2\kappa\sin\psi)\Delta\gamma^a + (\frac{4}{3}\mu - 2\kappa)\sin\psi\Delta\gamma^b \tag{2.61}$$

  In order to compute $\Delta\gamma^a$ and $\Delta\gamma^b$, we use two consistency conditions as follows:

$$f^a = \sigma_1^{\text{trial}} - \sigma_3^{\text{trial}} + (\sigma_1^{\text{trial}} + \sigma_3^{\text{trial}})\sin\phi - 2c\cos\phi - a\Delta\gamma^a - b\Delta\gamma^b = 0 \tag{2.62}$$

$$f^b = \sigma_1^{\text{trial}} - \sigma_2^{\text{trial}} + (\sigma_1^{\text{trial}} + \sigma_2^{\text{trial}})\sin\phi - 2c\cos\phi - b\Delta\gamma^a - a\Delta\gamma^b = 0 \tag{2.63}$$

  where

$$b = 2\mu(1+\sin\phi+\sin\psi-\frac{1}{3}\sin\phi\sin\psi) + 4\kappa\sin\phi\sin\psi \tag{2.64}$$

- **Return to the left edge:**
  The plastic flow vector on the left of the main plane reads as

$$\mathbf{N}^b := N^2 = (1+\sin\psi)\mathbf{e}_2 \otimes \mathbf{e}_2 - (1-\sin\psi)\mathbf{e}_3 \otimes \mathbf{e}_3 \tag{2.65}$$

Using Eq. (2.65), the principal stresses should be updated as:

$$\sigma_1 = \sigma_1^{\text{trial}} - (2\mu(1+\frac{1}{3}\sin\psi)+2\kappa\sin\psi)\Delta\gamma^a + (\frac{4}{3}\mu - 2\kappa)\sin\psi\Delta\gamma^b \quad (2.66)$$

$$\sigma_2 = \sigma_2^{\text{trial}} + (\frac{4}{3}\mu - 2\kappa)\sin\psi\Delta\gamma^a - (2\mu(1+\frac{1}{3}\sin\psi)+2\kappa\sin\psi)\Delta\gamma^b \quad (2.67)$$

$$\sigma_3 = \sigma_3^{\text{trial}} + (2\mu(1-\frac{1}{3}\sin\psi)-2\kappa\sin\psi)(\Delta\gamma^a + \Delta\gamma^b) \quad (2.68)$$

$$(2.69)$$

In order to compute $\Delta\gamma^a$ and $\Delta\gamma^b$, we use two consistency conditions as follows:

$$f^a = \sigma_1^{\text{trial}} - \sigma_3^{\text{trial}} + (\sigma_1^{\text{trial}} + \sigma_3^{\text{trial}})\sin\phi - 2c\cos\phi - a\Delta\gamma^a - b\Delta\gamma^b = 0 \quad (2.70)$$

$$f^b = \sigma_2^{\text{trial}} - \sigma_3^{\text{trial}} + (\sigma_2^{\text{trial}} + \sigma_3^{\text{trial}})\sin\phi - 2c\cos\phi - b\Delta\gamma^a - a\Delta\gamma^b = 0 \quad (2.71)$$

where

$$b = 2\mu(1-\sin\phi-\sin\psi-\frac{1}{3}\sin\phi\sin\psi)+4\kappa\sin\phi\sin\psi \quad (2.72)$$

3. **Return to the apex**:
   The principal stresses at the apex of the Mohr-Coulomb model are equal to the hydrostatic stress and thus the updated values should be

$$\boldsymbol{\sigma}_{n+1} := p_{n+1}\mathbf{I} \quad (2.73)$$

   where:
   p_{n+1} is the hydrostatic pressure and should be equal to the hydrostatic stress at the apex $p_{\text{apex}} = c\cot\phi$.

$$p_{n+1} = p_{\text{apex}} = c\text{cot}\phi \quad (2.74)$$

   which gives:

$$\sigma_1 = \sigma_2 = \sigma_3 = c\text{cot}\phi \quad (2.75)$$

The elastic predictor-plastic corrector scheme is shown in Algorithm 1 and the approach to selecting the appropriate return mapping, is summarised in a flowchart in Figure 2.11.

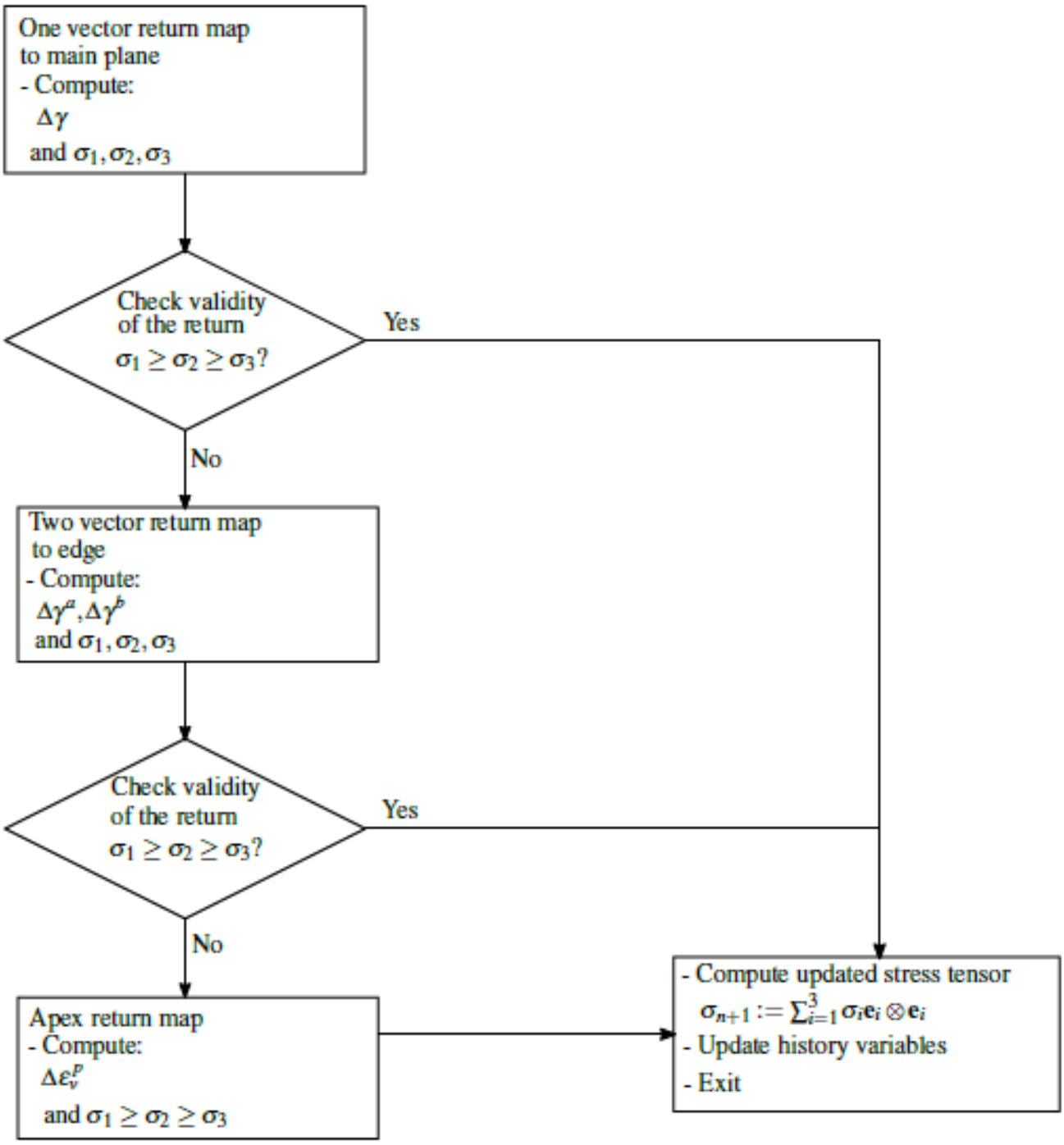

Fig. 2.11 Flowchart of selecting the appropriate return mapping, taken from [32]

Algorithm 1: Elastic predictor-plastic corrector algorithm according to [32]

1. Given the database and history variables $\boldsymbol{\varepsilon}_n^e$ at time t_n.
   Advance the strain to $\boldsymbol{\varepsilon}_{n+1}$ at time t_{n+1}
   $\Delta\boldsymbol{\varepsilon} = \boldsymbol{\varepsilon}_{n+1} - \boldsymbol{\varepsilon}_n$
2. Elastic predictor step
   $\boldsymbol{\varepsilon}_{n+1}^{e,\text{trial}} := \boldsymbol{\varepsilon}_n^e + \Delta\boldsymbol{\varepsilon}$
   $\boldsymbol{\sigma}_{n+1}^{\text{trial}} := 2\mu\,\text{dev}(\boldsymbol{\varepsilon}_{\text{n+1}}^{\text{e,trial}}) + \kappa\,\text{tr}(\boldsymbol{\varepsilon}_{\text{n+1}}^{\text{e,trial}})\mathbf{I}$
3. Spectral decomposition of the trial stresses
   Compute $(\sigma_1^{\text{trial}}, \sigma_2^{\text{trial}}, \sigma_3^{\text{trial}})$ such that
   $\sigma_1^{\text{trial}} \geq \sigma_2^{\text{trial}} \geq \sigma_3^{\text{trial}}$
4. Compute trial yield function and check for plastic loading
   $f^{\text{trial}} = \sigma_1^{\text{trial}} - \sigma_3^{\text{trial}} + (\sigma_1^{\text{trial}} + \sigma_3^{\text{trial}})\sin\phi - 2c\cos\phi$
   IF ($f^{\text{trial}} < 0$) THEN
   - This is an elastic step
   - set $(.)_{n+1} := (.)_{n+1}^{\text{trial}}$
   - GOTO 8

   ENDIF
5. Plastic corrector step with return mapping according to the flowchart in Figure 2.11
6. Map the updated stress tensor to the general stress space
   $\boldsymbol{\sigma}_{n+1} := \sum_{i=1}^{3} \sigma_i \mathbf{e}_i \otimes \mathbf{e}_i$
7. Update the history variable(elastic strain) $\boldsymbol{\varepsilon}_{n+1}^e := \frac{1}{2\mu}\text{dev}(\boldsymbol{\sigma}_{\text{n+1}}) + \frac{\text{tr}(\boldsymbol{\sigma}_{\text{n+1}})}{\kappa}\mathbf{I}$
8. EXIT

Consistent tangent modulus

An *algorithmically consistent* tangent modulus is necessary to obtain quadratic convergence for incremental-iterative solution of elasto-plasticity problems [93, 94]. An algorithmically consistent tangent modulus means that it is *consistent* with the stress update algorithm which is used. Therefore it can be written as

$$\mathbf{D}^{ep} := \frac{\text{d}\boldsymbol{\sigma}_{\text{n+1}}}{\text{d}\boldsymbol{\varepsilon}_{\text{n+1}}} \tag{2.76}$$

Since there are four mapping procedures for updating the stress, namely return to the main plane, right/left edges and the apex, there would also be four corresponding sets of

formulations for the consistent tangent modulus based on the derivatives of the updated principal stresses.

- **Return to the main plane**
  Differentiation of the corresponding updated principal stresses gives:

$$\mathrm{d}\sigma_1 = \mathrm{d}\sigma_1^{\mathrm{trial}} - (2\mu(1+\frac{1}{3}\sin\psi)+2\kappa\sin\psi)\mathrm{d}\Delta\gamma \tag{2.77}$$

$$\mathrm{d}\sigma_2 = \mathrm{d}\sigma_2^{\mathrm{trial}} + (\frac{4\mu}{3}-2\kappa)\sin\psi\mathrm{d}\Delta\gamma \tag{2.78}$$

$$\mathrm{d}\sigma_3 = \mathrm{d}\sigma_3^{\mathrm{trial}} + (2\mu(1-\frac{1}{3}\sin\psi)-2\kappa\sin\psi)\mathrm{d}\Delta\gamma \tag{2.79}$$

  $\mathrm{d}\Delta\gamma$ in the above equations is computed using the consistency condition

$$\tilde{f} = \mathrm{d}\sigma_1^{\mathrm{trial}} - \mathrm{d}\sigma_3^{\mathrm{trial}} + (\mathrm{d}\sigma_1^{\mathrm{trial}} + \mathrm{d}\sigma_3^{\mathrm{trial}})\sin\phi - a\mathrm{d}\Delta\gamma = 0 \tag{2.80}$$

  Here a is defined in Eq. (2.51).

- **Return to edges**
  The same way as in the case of main plane, the stress update formulae should be differentiated. $\mathrm{d}\Delta\gamma^a$ and $\mathrm{d}\Delta\gamma^b$ could be computed using the consistency conditions and the values should be substituted in the stress differentiation.

- **Return to the apex**

  Since the apex remains fixed in the stress space in perfect plasticity, the derivatives of the principal stresses vanish at the apex. Therefore:

$$\frac{\partial\sigma_i}{\partial\varepsilon_j} = 0 \qquad i,j = 1,2,3 \tag{2.81}$$

  which yields:

$$\mathbf{D}^{ep} = \mathbf{0} \tag{2.82}$$

reflecting the singularity at the apex.

2.7 Drucker-Prager plasticity model

The Drucker-Prager yield surface is a cone in the principal stress space as can be seen from Figure 2.12. It is defined as:

$$f = (3J_2)^{1/2} + \alpha p - k \tag{2.83}$$

For non-associated plasticity, a plastic potential function resembling the yield function is taken

$$g = (3J_2)^{1/2} + \beta p \tag{2.84}$$

α, k and β in the above equations are material parameters, known as the internal friction coefficient, the cohesion and the dilatancy factor. J_2 is the second invariant of deviatoric stresses and p is the hydrostatic pressure

$$p := \frac{1}{3}\mathrm{tr}\boldsymbol{\sigma} \tag{2.85}$$

J_2 and p can be expressed in compact matrix notation as

$$J_2 = \frac{1}{2}\boldsymbol{\sigma}^{\mathsf{T}}\mathbf{P}\boldsymbol{\sigma} \tag{2.86}$$

and

$$p = \boldsymbol{\sigma}^{\mathsf{T}}\boldsymbol{\pi} \tag{2.87}$$

using the projection matrix $\boldsymbol{P}$ and the projection vector π defined as

$$\mathbf{P} = \begin{bmatrix} 2/3 & -1/3 & -1/3 & 0 \\ -1/3 & 2/3 & -1/3 & 0 \\ -1/3 & -1/3 & 2/3 & 0 \\ 0 & 0 & 0 & 2 \end{bmatrix} \tag{2.88}$$

and

$$\boldsymbol{\pi}^{\mathsf{T}} = [1/3, 1/3, 1/3, 0] \tag{2.89}$$

The yield function, Eq. (3.34) can be rewritten as

$$f = [\frac{3}{2}\boldsymbol{\sigma}^{\mathsf{T}}\mathbf{P}\boldsymbol{\sigma}]^{1/2} + \alpha\boldsymbol{\sigma}^{\mathsf{T}}\boldsymbol{\pi} - k \tag{2.90}$$

Similarly for the plastic potential, we have

$$g = [\frac{3}{2}\boldsymbol{\sigma}^{\mathsf{T}}\mathbf{P}\boldsymbol{\sigma}]^{1/2} + \beta\boldsymbol{\sigma}^{\mathsf{T}}\boldsymbol{\pi} \tag{2.91}$$

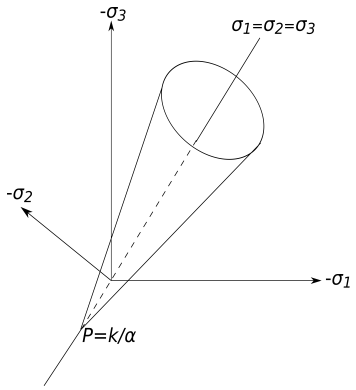

Fig. 2.12 Drucker-Prager yield surface in principal stress state

The normals to the yield surface and plastic potential contour are:

$$\mathbf{M} = \left[\frac{3\mathbf{P}\boldsymbol{\sigma}}{2\sqrt{3/2\boldsymbol{\sigma}^{\mathsf{T}}\mathbf{P}\boldsymbol{\sigma}}} + \alpha\boldsymbol{\pi} \right] \tag{2.92}$$

and

$$\mathbf{N} = \left[\frac{3\mathbf{P}\boldsymbol{\sigma}}{2\sqrt{3/2\boldsymbol{\sigma}^{\mathsf{T}}\mathbf{P}\boldsymbol{\sigma}}} + \beta\boldsymbol{\pi} \right] \tag{2.93}$$

The material parameters can be chosen in such a way that the Mohr-Coulomb yield surface is approximated at different locations [32]. For a match to the three outermost corners :

$$\alpha = \frac{6\sin\phi}{3-\sin\phi} \quad ,\beta = \frac{6\sin\psi}{3-\sin\psi} \quad ,k = \frac{6c\cos\phi}{3-\sin\phi} \tag{2.94}$$

For a match to the inner corners:

$$\alpha = \frac{6\sin\phi}{3+\sin\phi} \quad ,\beta = \frac{6\sin\psi}{3+\sin\psi} \quad ,k = \frac{6c\cos\phi}{3-\sin\phi} \tag{2.95}$$

And another set to match the plane strain conditions:

$$\alpha = \frac{3\sqrt{3}\tan\phi}{\sqrt{9+12\tan^2\phi}} \quad ,\beta = \frac{3\sqrt{3}\tan\psi}{\sqrt{9+12\tan^2\psi}} \quad ,k = \frac{3\sqrt{3}c}{\sqrt{9+12\tan^2\phi}} \tag{2.96}$$

2.7.1 Numerical implementation

Compared to the Mohr-Coulomb model, the integration of the rate equations in the Drucker-Prager model is much easier. This is mainly due to the fact that the yield surface of the Drucker-Prager model has only one point of singularity, namely the apex, which needs special care.

Stress update procedure

Here, again a general return mapping is considered to update the stress state as in [28].

1. **Return to the main plane**

   Elastic Predictor step
   The trial stress state is computed as in Eq. (2.10). Inserting the value of trial stresses in Eq. (2.90), gives the value for trial yield function as:

$$f^{\text{trial}} = [\frac{3}{2}\boldsymbol{\sigma}_{n+1}^{\text{trial}\,\mathsf{T}}\mathbf{P}\boldsymbol{\sigma}_{n+1}^{\text{trial}}]^{1/2} + \alpha\boldsymbol{\sigma}_{n+1}^{\text{trial}\,\mathsf{T}}\boldsymbol{\pi} - k \tag{2.97}$$

   Now if the value of f^{trial} is negative, then the assumption of elastic state was correct, otherwise a plastic corrector step is needed to return the stress state on the yield surface.

   Plastic Corrector step
   In case the yield criterion is violated, the material has gone through plastic deformation. The incremental plastic multiplier is integrated by backward Euler as in Eq. (2.11). Since the vectors $\mathbf{M}$ and $\mathbf{N}$ are normals to the yield and plastic potential surfaces, respectively, their trial values could be used instead of their updated values. So:

$$\Delta\gamma = \frac{\mathbf{M}_{n+1}^{\text{trial}} : \mathbf{D}^e : \Delta\boldsymbol{\varepsilon}_{n+1}}{\mathbf{M}_{n+1}^{\text{trial}} : \mathbf{D}^e : \mathbf{N}_{n+1}^{\text{trial}}} \tag{2.98}$$

   With $\mathbf{M}_{n+1}^{\text{trial}}$ and $\mathbf{N}_{n+1}^{\text{trial}}$ being computed as

$$\mathbf{M}_{n+1}^{\text{trial}} = \left[\frac{3\mathbf{P}\boldsymbol{\sigma}_{n+1}^{\text{trial}}}{2\sqrt{3/2\boldsymbol{\sigma}_{n+1}^{\text{trial}\,\mathsf{T}}\mathbf{P}\boldsymbol{\sigma}_{n+1}^{\text{trial}}}} + \alpha\boldsymbol{\pi}\right] \tag{2.99}$$

   and

$$\mathbf{N}_{n+1}^{\text{trial}} = \left[\frac{3\mathbf{P}\boldsymbol{\sigma}_{n+1}^{\text{trial}}}{2\sqrt{3/2\boldsymbol{\sigma}_{n+1}^{\text{trial}\,\mathsf{T}}\mathbf{P}\boldsymbol{\sigma}_{n+1}^{\text{trial}}}} + \beta\boldsymbol{\pi} \right] \tag{2.100}$$

The plastic strain increment is computed by Eq. (2.12) and using $\mathbf{N}$:

$$\Delta\boldsymbol{\varepsilon}_{n+1}^{p} = \Delta\gamma\mathbf{N}_{n+1}^{\text{trial}} \tag{2.101}$$

The stresses are updated using Eq. (2.16). Finally the plastic strains are also updated.

2. **Return to the apex**
   The Drucker-Prager yield surface is singular at the apex. The stress state at the apex is

$$\|\text{dev}\boldsymbol{\sigma}\| = \mathbf{0} \quad , p_{\text{apex}} = \frac{k}{\alpha} \tag{2.102}$$

   In the return mapping algorithm adopted here, it is first assumed that the stress state should be returned to the smooth part of the yield surface. If the updated stresses violate the condition below, it means that the assumption was not correct and the stress should be returned to the apex.

$$\alpha\boldsymbol{\sigma}_{n+1}^{\text{T}}\boldsymbol{\pi} < k \tag{2.103}$$

   The updated stresses and plastic strain increments at the apex read as:

$$\boldsymbol{\sigma}_{n+1} = \frac{3k}{\alpha}\boldsymbol{\pi}^{\text{T}} \tag{2.104}$$

$$\Delta\boldsymbol{\varepsilon}_{n+1}^{p} = \mathbf{D}^{e-1} : (\boldsymbol{\sigma}_{n+1}^{\text{trial}} - \boldsymbol{\sigma}_{n+1}) \tag{2.105}$$

Consistent tangent modulus

- **Return to the main plane**
  From Eq. (2.16), the updated stresses read as:

$$\boldsymbol{\sigma}_{n+1} = \boldsymbol{\sigma}_{n+1}^{\text{trial}} - \mathbf{D}^{e}\Delta\gamma\mathbf{N}_{n+1} \tag{2.106}$$

  Differentiating Eq. (2.106) yields:

$$\dot{\boldsymbol{\sigma}} = \mathbf{H}_{n+1}\left[\dot{\boldsymbol{\varepsilon}} - \dot{\gamma}\mathbf{N}_{n+1}\right] \tag{2.107}$$

where

$$\mathbf{H}_{n+1}^{-1} = [\mathbf{D}^e]^{-1} + \Delta\gamma\sqrt{\frac{3}{2}}\frac{\boldsymbol{\sigma}_{n+1}^{\mathsf{T}}\mathbf{P}\boldsymbol{\sigma}_{n+1}\mathbf{P} - \mathbf{P}\boldsymbol{\sigma}_{n+1}\boldsymbol{\sigma}_{n+1}^{\mathsf{T}}\mathbf{P}}{\sqrt{\boldsymbol{\sigma}_{n+1}^{\mathsf{T}}\mathbf{P}\boldsymbol{\sigma}_{n+1}}} \tag{2.108}$$

Inserting Eq. (2.8) into Eq. 2.107 gives:

$$\dot{\boldsymbol{\sigma}} = \left[\mathbf{H}_{n+1} - \frac{\mathbf{H}_{n+1}\mathbf{N}_{n+1}(\mathbf{M}_{n+1})^{\mathsf{T}}\mathbf{H}_{n+1}}{(\mathbf{M}_{n+1})^{\mathsf{T}}\mathbf{H}_{n+1}\mathbf{N}_{n+1}}\right]\dot{\boldsymbol{\varepsilon}} \tag{2.109}$$

which gives an explicit form for the consistent tangential modulus:

$$\mathbf{D}^{ep} = \left[\mathbf{H}_{n+1} - \frac{\mathbf{H}_{n+1}\mathbf{N}_{n+1}(\mathbf{M}_{n+1})^{\mathsf{T}}\mathbf{H}_{n+1}}{(\mathbf{M}_{n+1})^{\mathsf{T}}\mathbf{H}_{n+1}\mathbf{N}_{n+1}}\right] \tag{2.110}$$

The above equation can be used for the smooth portion of the yield cone.

- **Return to the apex**
  The stress tensor at the apex consists only of principal stresses. Since the apex remains fixed in the stress space in perfect plasticity, the derivatives of the principal stresses vanish at the apex. Therefore:

$$\mathbf{D}^{ep} = \mathbf{0} \tag{2.111}$$

  reflecting the singularity at the apex as in the Mohr-Coulomb model.

2.8 Verification examples

2.8.1 Single element in tension

An element of material with unit dimensions is considered in tension under plane strain conditions. The geometry and the boundary conditions are depicted in Figure 2.13. This element is simulated with the Mohr-Coulomb model and its corresponding Drucker-Prager model with plane strain, inner cone and outer cone matches. The material parameters are shown in tables 2.2 and 2.3. A cyclic displacement load as shown in Figure 2.14a is prescribed on top of the element.

Analytical solution

The state of stress and strain for the element can be simply computed analytically in the elastic regime and therefore it is possible to determine the analytical longitudinal stress and

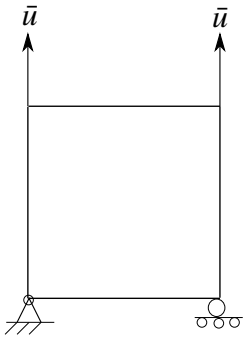

Fig. 2.13 Geometry and boundary conditions of the single element test

Table 2.2 Parameters used for the Mohr-Coulomb model in Figure 2.13

Parameter	M-C model
E	100 MPa
ν	0.3
ϕ	20^o
ψ	20^o
c	100 KPa

Table 2.3 Parameters used for the Drucker-Prager model in Figure 2.13

Parameter	Plane strain match	Inner corners match	Outer corners match
E	100 MPa	100 MPa	100 MPa
ν	0.3	0.3	0.3
α	0.582	0.61	0.77
β	0.582	0.61	0.77
k	159.7 KPa	168.8 KPa	212.1 KPa

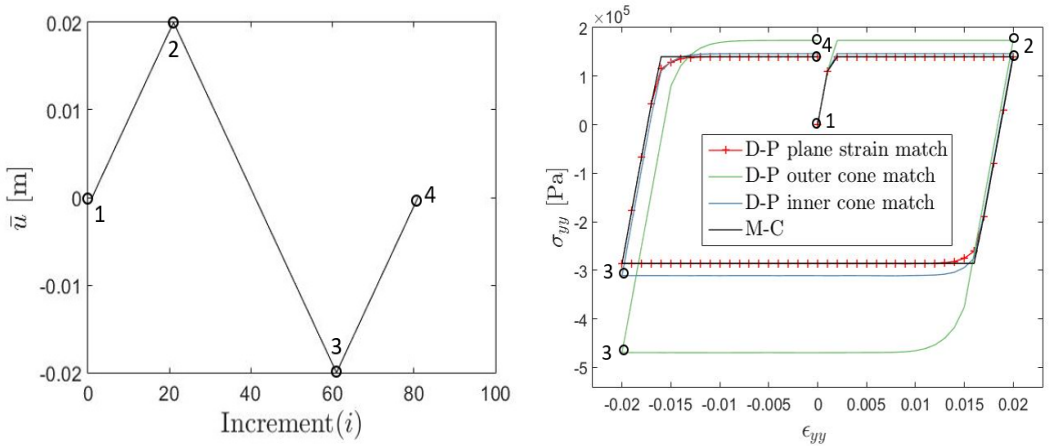

(a) Cyclic prescribed displacement load (b) Stress *vs* strain

Fig. 2.14 Single element test in tension

strain at which plasticity first starts.
From the plane strain assumption, $\varepsilon_z = 0$, it follows:

$$\sigma_z = \nu(\sigma_x + \sigma_y) \tag{2.112}$$

With the imposed boundary conditions

$$\sigma_x = 0 \tag{2.113}$$

Therefore we have

$$\varepsilon_x = -\frac{\nu}{(1-\nu)}\varepsilon_y \tag{2.114}$$

and

$$\sigma_z = \nu\sigma_y \tag{2.115}$$

The longitudinal stress also reads

$$\sigma_y = \frac{E}{(1-\nu^2)}\varepsilon_y \tag{2.116}$$

On the other hand

$$\sqrt{3J_2} = \sqrt{\frac{(\sigma_x-\sigma_y)^2 + (\sigma_y-\sigma_z)^2 + (\sigma_z-\sigma_x)^2 + 6\sigma_{xy}^2}{2}} \tag{2.117}$$

which simplifies to

$$\sqrt{3J_2} = \frac{E\sqrt{(1-\nu+\nu^2)}}{(1-\nu^2)}\varepsilon_y \tag{2.118}$$

And we also have

$$p = \frac{1}{3}(\sigma_x + \sigma_y + \sigma_z) \tag{2.119}$$

which reduces to

$$p = \frac{E}{3(1-\nu)}\varepsilon_y \tag{2.120}$$

Now we can write the yield function in terms of ε_y only as

$$f = \frac{E\sqrt{(1-\nu+\nu^2)}}{(1-\nu^2)}\varepsilon_y + \alpha\frac{E}{3(1-\nu)}\varepsilon_y - k \tag{2.121}$$

Plasticity begins when $f \geq 0$, so the root to the above equation is the longitudinal strain at which plasticity starts

$$\varepsilon_y = 0.001273 \tag{2.122}$$

The corresponding longitudinal stress value for the Mohr-Coulomb and a plane strain matched Drucker-Prager criteria is

$$\sigma_y = 1.398 \times 10^5 \text{ Pa} \tag{2.123}$$

These values completely match with the FE simulation results shown in Figure 2.14b.

2.8.2 Smooth rigid strip footing in plane strain conditions

Computation of the bearing capacity of a rigid footing belongs to difficult problems in elasto-plastic finite element analysis as there are large stress gradients and discontinuities at the footing edge. Therefore it is a very good example to verify the formulations and algorithms implemented.

In Figure 2.15a, the geometry and boundary conditions of the footing problem are shown. The model is meshed with 975 second order quadrilateral elements as can be seen in Figure 2.15b. r is considered to be 0.5 m. Simulations are carried out with the Mohr-Coulomb and its corresponding Drucker-Prager model with plane strain match. Two cases are simulated: associated and non-associated, with $\psi = 20^\circ$ and $\psi = 10^\circ$, respectively. The strip is subject to an increasing displacement load from 0 to 140 mm. The material parameters are summarised in tables 2.4 and 2.5. The theoretical limit for this problem is given by Prandtl [75] as:

$$p = c(\tan^2(\pi/4 + \phi/2)\exp^{\pi\tan(\phi)} - 1)\cot(\phi) \tag{2.124}$$

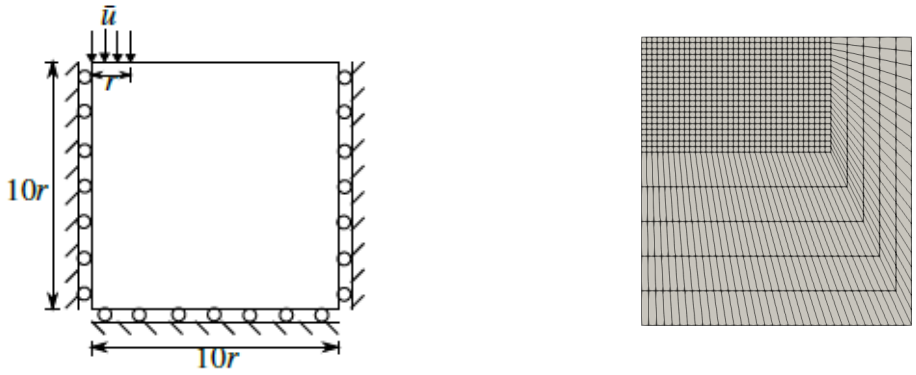

(a) Geometry and boundary conditions (b) Mesh

Fig. 2.15 Model of the rigid strip footing

Table 2.4 Parameters used for the Mohr-Coulomb model in Figure 2.15

Parameter	M-C model
E	100 MPa
ν	0.3
ϕ	20^o
ψ	$20^o/10^o$
c	100 KPa

Table 2.5 Parameters used for the Drucker-Prager model in Figure 2.15

Parameter	D-P model
E	100 MPa
ν	0.3
α	0.582
β	0.582/0.3
k	159.7 KPa

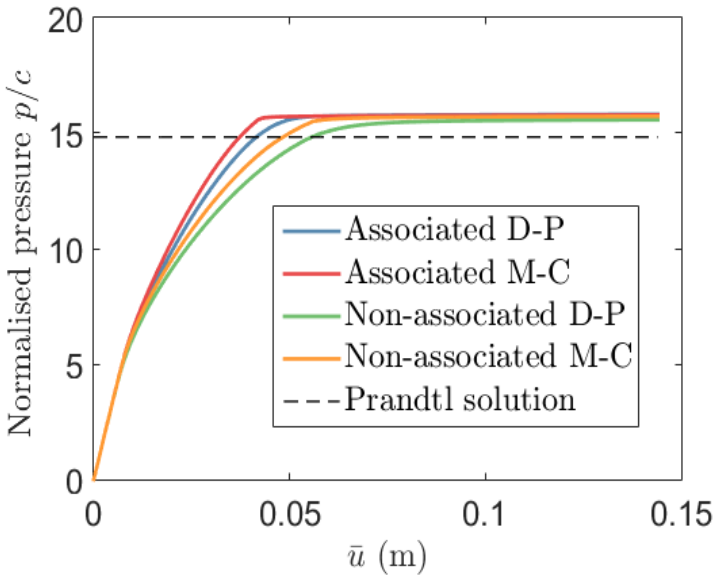

Fig. 2.16 Normalised pressure *vs* settlement

For $\phi = 20°$, the normalized theoretical limit pressure is $(p/c) = 14.84$. In Figure 2.16, the simulation results for both associated and non-associated cases are shown and they agree rather well with the theoretical limit solution. The contours of equivalent plastic strains are illustrated in Figure 2.17. as can be seen, there is high plastic deformation at the edge of the footing and shear bands form as well.

2.9 Background to localisation and mesh dependency in numerical simulations

In the 1970s it was observed that the introduction of strain softening in constitutive relations caused a phenomenon now known as mesh dependence or mesh sensitivity. While it is normal that, upon refinement of the discretisation, the numerical solution approaches the correct solution of the initial value problem, the connotations mesh dependence or mesh sensitivity are typically reserved for a phenomenon where the solution does not seem to be able to ever converge to the correct solution where there is singularity or a solution is found which does not seem physically realistic. This is most simply shown at hand of a one-dimensional bar loaded in tension [28], as shown in Figure 2.18 and composed of a material exhibiting strain softening behaviour as can be seen from Figure 2.19a. The bar is meshed with m elements. A linear relationship exists between the axial stress σ and axial

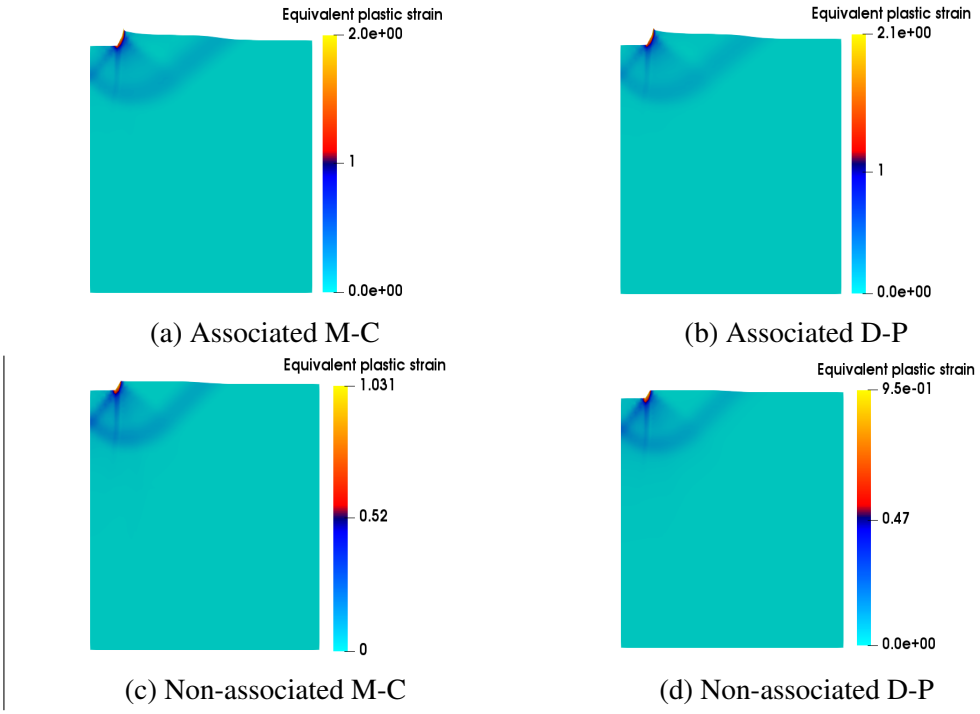

(a) Associated M-C (b) Associated D-P

(c) Non-associated M-C (d) Non-associated D-P

Fig. 2.17 Contours of equivalent plastic strains at $\bar{u} = 0.12$m

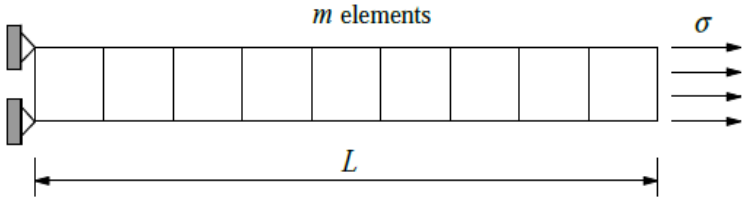

Fig. 2.18 1D bar with length L in tension, taken from [28]

strain ε up to reaching the tensile strength f_t:

$$\sigma = E\varepsilon \tag{2.125}$$

where E is the Young's modulus. Upon reaching the peak strength, the material starts to damage at the axial strain value of κ_i and becomes fully damaged at the value of κ_u, where it loses its load-carrying capacity. The constitutive material law in the post-peak regime reads:

$$\sigma = f_t + h(\varepsilon - \kappa_i) \tag{2.126}$$

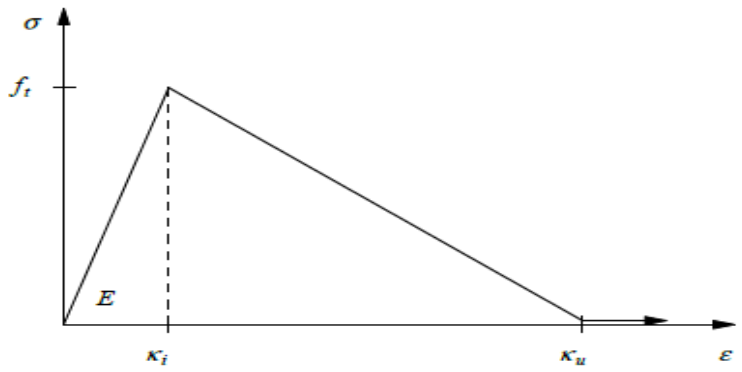

(a) Elastic-linear damage material law

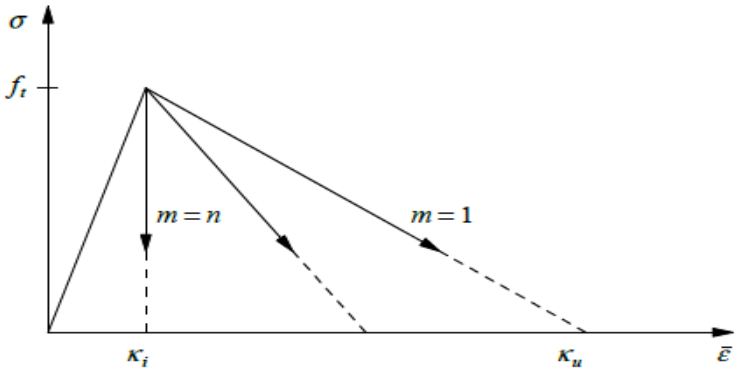

(b) Stress-average strain curve of the bar with imperfection

Fig. 2.19 Constitutive law and the response of the bar, taken from [28]

For damaging materials, h is called the softening modulus and is negative. For the linear damaging law at hand, we have:

$$h = -\frac{f_t}{k_u - k_i} \tag{2.127}$$

Now we assume that there is an imperfect element in the bar with a slightly lower tensile strength compared to the rest of the $m-1$ elements. This element will reach the peak stress and fail sooner than others. Therefore, $m-1$ elements will be elastically unloading while the imperfect element is going through damage. The average strain in the bar is given as:

$$\bar{\varepsilon} = \frac{1}{m}\left[\frac{\sigma - f_t + h\kappa_i}{h} + (m-1)\frac{\sigma}{\varepsilon}\right] \tag{2.128}$$

Inserting Eq. (2.127) into Eq. (2.128) yields:

$$\bar{\varepsilon} = \frac{\sigma}{E} + \frac{n(f_t - \sigma)}{mE} \tag{2.129}$$

where $n = \kappa_u/\kappa_i$.

The pathological mesh size dependency can now easily be observed from Eq. (2.129) and is plotted in Figure 2.19b. Upon refinement of the discretisation, the post-peak descending branch runs steeper and steeper, giving a more and more brittle structural response. Beyond a certain number of elements a snap-back phenomenon is observed, and the overall displacement decreases after passing the peak load. In the limit of an infinitely dense mesh ($m \to \infty$), the post-peak load-displacement curve doubles back on its original (elastic) loading branch, resulting in the physically unrealistic case of failure without energy dissipation [28].

While this phenomenon has originally been ascribed to shortcomings of the finite element formulation, the true reason appeared to be the loss of well-posedness of the initial or boundary-value problem, and thus emerges for *any* discretisation method [76, 68]. Indeed, quasi-static problems become ill-posed at a certain stage of the loading process and failure takes place at a discrete, characteristic plane. The observed mesh dependence is then just a manifestation of the inability of the discretisation method to exactly capture a discrete plane. Hadamard was the first to conduct an analytical study into localisation for elastic solids and has identified the loss of well-posedness as the underlying reason [41]. Extensions to plastic deformations have been made in [44, 53, 100].

Localisation occurs commonly in the form of narrow, highly deformed zones, known as shear bands in a wide range of materials, e.g. in concrete [102], metals [15, 20, 22] and geomaterials [83, 89, 103, 105, 114, 115]. Shear bands are considered to emerge from a material instability, i.e. as a bifurcation from a homogeneous deformation into a deformation mode that involves a discontinuity. Numerical simulations of localised deformation can run into problems, in particular a pathological mesh dependence, and severe difficulties, or even an impossibility, to obtain converged solutions as reported in [14, 17, 52, 54].

It has been recognised that strain softening is not the only material instability which can lead to loss of well-posedness. Indeed, it has also been demonstrated for strain-*rate* softening [113]. The non-associated plastic flow has also been shown to have a materially destabilising effect and can cause the boundary-value problem to become ill-posed [53, 84, 80, 65, 79, 104, 108]. In principle, non-associated flow can therefore also induce structural softening and mesh sensitivity, but with some exceptions [24, 50, 48], little attention has been given in the literature to the possibility of this phenomenon to occur.

The pathological mesh dependence of numerical results is not limited to only mesh size but also includes the mesh orientation which results from the application of a non-associated flow rule. While the effect of mesh orientation has received less attention than the effect which mesh densification can have in localisation problems, its relevance has been documented for strain softening [96], for strain-rate softening in the formation of Portevin-Le

Chatelier bands [113] and for softening-rehardening as occurs in Lüders band formation [56].

2.10 Loss of uniqueness of the solution

A mathematical model of a physical problem is reliable only when the initial or boundary value problem is well-posed. A problem is well-posed when it has a solution which is unique and the solution continuously depends on the data. We now investigate conditions under which a body which is modelled using non-associated elasto-plasticity, loses well-posedness, therefore opening up the possibility of strain localisation to occur. We consider quasi-static loading conditions and postulate the existence of a solution which is discontinuous across a (possibly curved) plane Γ_d as shown in Figure 2.20. Assuming a linear comparison solid [43], so that the tangential stiffness tensor $\mathbf{D}$ is identical at both sides of the discontinuity, the jump in the stress rate is related to the jump in the strain rate as:

$$[\![\dot{\boldsymbol{\sigma}}]\!] = \mathbf{D} : [\![\dot{\boldsymbol{\varepsilon}}]\!] \tag{2.130}$$

The jump in the traction rate, $[\![\dot{\mathbf{t}}_d]\!]$, across the plane is expressed as:

$$[\![\dot{\mathbf{t}}_d]\!] = \mathbf{n}_{\Gamma_d} \cdot [\![\dot{\boldsymbol{\sigma}}]\!] \tag{2.131}$$

where $\mathbf{n}_{\Gamma_d}$ is the normal vector to the discontinuity Γ_d. Using the expression for $[\![\dot{\boldsymbol{\sigma}}]\!]$ given by Eq. (2.130), the jump in the traction rate reads:

$$[\![\dot{\mathbf{t}}_d]\!] = \mathbf{n}_{\Gamma_d} \cdot \mathbf{D} : [\![\dot{\boldsymbol{\varepsilon}}]\!] \tag{2.132}$$

A velocity field $\dot{\mathbf{u}}$ which contains a discontinuity at Γ_d can generally be expressed as:

$$\dot{\mathbf{u}} = \dot{\tilde{\mathbf{u}}} + \mathscr{H}_{\Gamma_d} \dot{\hat{\mathbf{u}}} \tag{2.133}$$

where $\mathscr{H}_{\Gamma_d}$ is the Heaviside function, and $\dot{\tilde{\mathbf{u}}}$ and $\dot{\hat{\mathbf{u}}}$ are continuous velocity fields on both sides of the discontinuity. Differentiating Eq. (2.133) results in the strain rate field:

$$\dot{\boldsymbol{\varepsilon}} = \nabla^{\mathrm{sym}} \dot{\tilde{\mathbf{u}}} + \mathscr{H}_{\Gamma_d} \nabla^{\mathrm{sym}} \dot{\hat{\mathbf{u}}} + \delta_{\Gamma_d} (\dot{\hat{\mathbf{u}}} \otimes \mathbf{n}_{\Gamma_d})^{\mathrm{sym}} \tag{2.134}$$

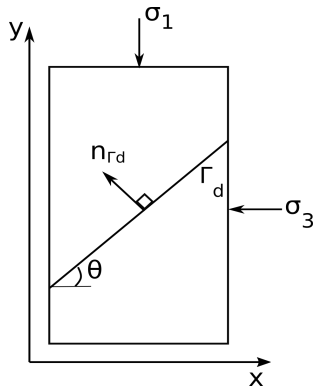

Fig. 2.20 Discontinuity plane Γ_d in a 2D continuum

where $(.)^{\text{sym}}$ refers to the symmetrised part of the operator and δ_{Γ_d} denotes the Dirac function at Γ_d. The strain rate jump at Γ_d can be written as:

$$[\![\dot{\boldsymbol{\varepsilon}}]\!] = \zeta \left(\dot{\tilde{\mathbf{u}}} \otimes \mathbf{n}_{\Gamma_d}\right)^{\text{sym}} \tag{2.135}$$

with ζ a non-zero scalar representing the magnitude of the difference in the strain rate jump. Substitution into Eq. (2.132) and exploiting the minor symmetry of $\mathbf{D}$ yields:

$$[\![\dot{\mathbf{t}}_d]\!] = \zeta \left(\mathbf{n}_{\Gamma_d} \cdot \mathbf{D} \cdot \mathbf{n}_{\Gamma_d}\right) \cdot \dot{\tilde{\mathbf{u}}} \tag{2.136}$$

A non-trivial solution ($\zeta \neq 0$) to Eq. (2.136) exists if and only if $\mathbf{n}_{\Gamma_d} \cdot \mathbf{D} \cdot \mathbf{n}_{\Gamma_d}$ is singular:

$$\det\left(\mathbf{n}_{\Gamma_d} \cdot \mathbf{D} \cdot \mathbf{n}_{\Gamma_d}\right) = 0 \tag{2.137}$$

Eq. (2.137) is the condition for the existence of discontinuous, localised solutions and also determines the speed at which plane acceleration waves in solids vanish [44].

2.10.1 Application to non-associated plasticity

Here the Mohr-Coulomb plasticity model is considered for the analysis. The yield function and plastic potential are given here once more for completeness:

$$f = \frac{1}{2}(\sigma_1 - \sigma_3) + \frac{1}{2}(\sigma_1 + \sigma_3)\sin\phi - c\cos\phi \tag{2.138}$$

$$g = \frac{1}{2}(\sigma_1 - \sigma_3) + \frac{1}{2}(\sigma_1 + \sigma_3)\sin\psi \tag{2.139}$$

Herein, σ_1 and σ_3 are the largest and the smallest principal stresses, respectively, while ϕ, ψ and c are the friction angle, the dilation angle and the cohesion, respectively.

For a Mohr-Coulomb plasticity model with a non-associated flow rule as above, the hardening modulus h has been derived in [7, 8, 11–13, 23, 84, 107, 109]. They all result in the same relationship which will be derived and discussed here. The continuum tangent modulus is given by:

$$\mathbf{D}^{ep} = \left[\mathbf{D}^{e} - \frac{\mathbf{D}^{e}\mathbf{N}(\mathbf{M})^{\mathsf{T}}\mathbf{D}^{e}}{h + (\mathbf{M})^{\mathsf{T}}\mathbf{D}^{e}\mathbf{N}}\right] \tag{2.140}$$

Where $\mathbf{D}^{e}$ is the elastic stiffness matrix, h is the hardening modulus, $\mathbf{M}$ and $\mathbf{N}$ are the derivatives of the yield and plastic potential functions. Substituting Eq. (2.140) into Eq. (2.137) yields:

$$\begin{aligned}\frac{h}{\mu} &= 4\mathbf{n}_{\Gamma_d}\cdot\mathbf{N}\cdot\mathbf{M}\cdot\mathbf{n}_{\Gamma_d} - 2(\mathbf{n}_{\Gamma_d}\cdot\mathbf{N}\cdot\mathbf{n}_{\Gamma_d})(\mathbf{n}_{\Gamma_d}\cdot\mathbf{M}\cdot\mathbf{n}_{\Gamma_d}) - 2\mathbf{N}\colon\mathbf{M} \\ &\quad - 2\frac{\nu}{(1-\nu)}(\mathbf{n}_{\Gamma_d}\cdot\mathbf{N}\cdot\mathbf{n}_{\Gamma_d} - \mathrm{tr}(\mathbf{N}))(\mathbf{n}_{\Gamma_\mathrm{d}}\cdot\mathbf{M}\cdot\mathbf{n}_{\Gamma_\mathrm{d}} - \mathrm{tr}(\mathbf{M}))\end{aligned} \tag{2.141}$$

where μ and ν are the shear modulus and Poisson's ratio, respectively.
Components of $\mathbf{n}_{\Gamma_d}$, $\mathbf{M}$ and $\mathbf{N}$ in the principal directions can be computed as follows:

$$\begin{aligned}(n_{\Gamma_d})_1 &= \sin\theta \\ (n_{\Gamma_d})_2 &= 0 \\ (n_{\Gamma_d})_3 &= \cos\theta\end{aligned} \tag{2.142}$$

θ is the angle between the most compressive principal stress and the localised shear band.

$$\begin{aligned}M_1 &= 1+\sin\phi \\ M_2 &= 0 \\ M_3 &= -(1-\sin\phi)\end{aligned} \tag{2.143}$$

$$\begin{aligned}N_1 &= 1+\sin\psi \\ N_2 &= 0 \\ N_3 &= -(1-\sin\psi)\end{aligned} \tag{2.144}$$

Eq. (2.141) can therefore be simplified as:

$$\frac{h}{\mu} = \frac{(\sin\phi-\sin\psi)^2 - (2\cos 2\theta - \sin\psi - \sin\phi)^2}{8(1-\nu)} \tag{2.145}$$

Eq. (2.145) is a relation between the hardening modulus and the orientation of a discontinuity in the solution for a given set of material parameters μ, ν, ϕ, ψ. h is positive for hardening and is a decreasing function of plastic strain for softening. Therefore, the earliest loading level at which the softening occurs and shear bands might emerge is at peak. By setting the derivative of h with respect to θ, equal to zero, the maximum value of hardening modulus, h_{crit} , can be computed:

$$\frac{h_{\text{crit}}}{\mu} = \frac{(\sin\phi - \sin\psi)^2}{8(1-\nu)} \tag{2.146}$$

With Eq. (2.146), we can examine the conditions which lead to a real solution for h_{crit}, opening up the possibility of mesh sensitive solutions.

For the particular case of a non-associated Mohr-Coulomb elastic-perfectly plastic model, we have $h = 0$ and since $\mu > 0$ and $\nu \leq 1/2$, a range of angles θ can be found for which $h < h_{\text{crit}}$ for non-associated flow, i.e. when $\psi < \phi$. These angles are usually bounded by the classical Coulomb and Roscoe angles, introduced in [21, 83], which are the roots of the hardening modulus. This is visualised in Figure 2.21 for a given set of material parameters ($\nu = 0.25$ and $\phi = 25^{\text{o}}$).

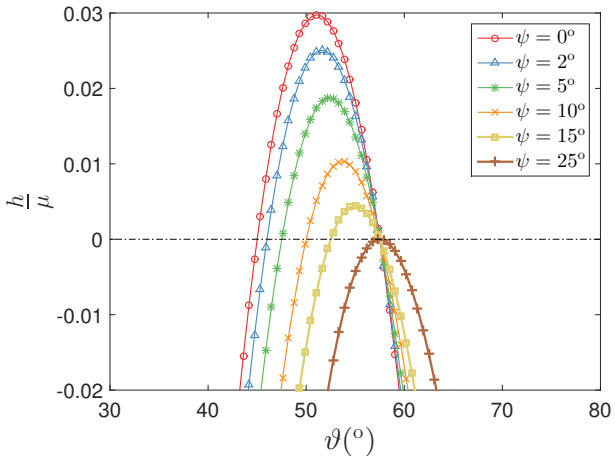

Fig. 2.21 Hardening modulus *vs* the orientation angle of the shear band, $\vartheta = \pi/2 - \theta$

2.10.2 The orientation of shear bands

There are three main approaches to compute the inclination angle of the shear bands. Coulomb considered the orientation angle to be $\theta = 45^{\text{o}} - \phi/2$ in [21] . Roscoe has derived another solution, namely $\theta = 45^{\text{o}} - \psi/2$ in [83], which gives prominence to role of the dilatancy. Another relation, $\theta = 45^{\text{o}} - (\psi + \phi)/4$, was based on experimental data [5]. This relation was also found in experiments on Karlsruhe sand and in an accompanying bifurcation analysis

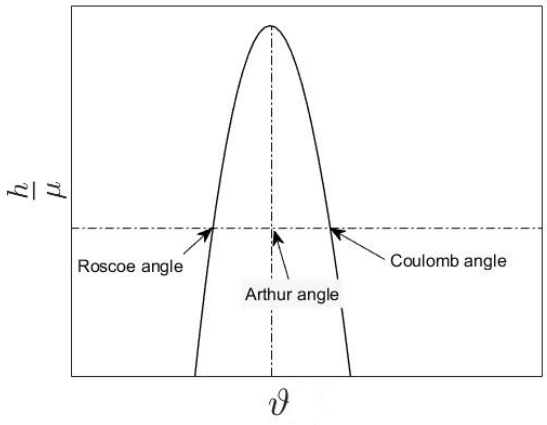

Fig. 2.22 Classical inclination angles of shear bands

[104]. These values also come out of the previous localisation analysis as the roots and the abscissa for the maximum of Eq. (2.145) and are shown in Figure 2.22. For associated plasticity ($\psi = \phi$), all these angles coincide with each other and therefore, the shear band has a unique inclination angle. According to [6, 46], the shear band angle varies between the Roscoe and the Coulomb solutions depending on the mean particle size based on analysis of a wide range of experimental data. For coarse-grained sands the Roscoe solution is approached, while for finer grains the Coulomb solution tends to be favoured. These findings were corroborated theoretically [108], and experimentally for specimens with coarse-sized particles [38] and for fine sands [33].

Chapter 3

Cosserat continuum mechanics

3.1 Introduction to the Cosserat theory

Cosserat theory belongs to continuum models, i.e. the microstructure is implicitly taken into account in the equivalent continuum. The basis of the Cosserat continuum model was first mentioned by the Cosserat brothers in [19]. A Cosserat continuum is a manifold of rigid crosses (oriented rigid particles) where additional degrees of freedom to account for micro-rotations are included. Another feature of the Cosserat continuum is the internal length parameter which is determined by the length scale of a representative elementary volume. Simulation of the localisation of shear bands in granular materials was among the first numerical applications of the Cosserat theory [25, 26, 34, 63, 98]. In this chapter, the

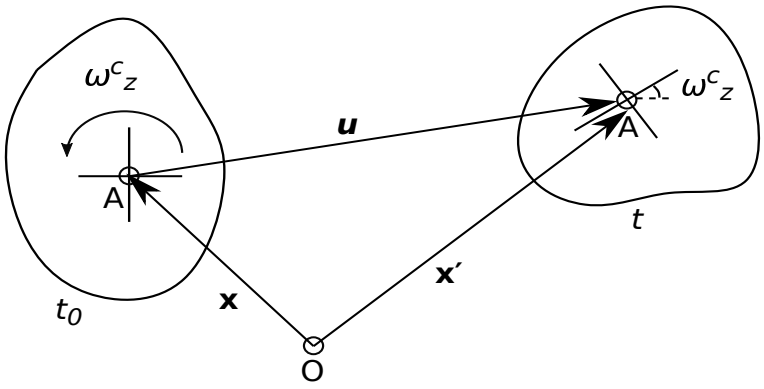

Fig. 3.1 A material point in a 2D Cosserat medium

governing equations for a 2D Cosserat continuum are discussed and useful measures for the description of the motion of the continuum are introduced. For more details, the reader is referred to [2, 27, 97, 106].

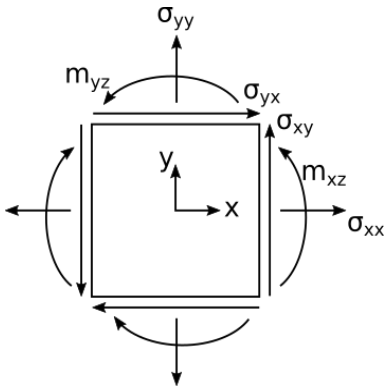

Fig. 3.2 Stresses and couple stresses on an element of material in a 2D Cosserat medium

3.2 Numerical implementation of Cosserat continuum mechanics for 2D condition

In this section, an overview of the numerical implementation procedure of a 2D isotropic Cosserat continuum plasticity model is discussed [25, 26, 90]. A 2-D plane strain continuum is considered here in the $x-y$ plane. A rotational degree of freedom ω_z^c around the z axis is also introduced as shown in Figure 3.1. The displacement vector is defined as:

$$\boldsymbol{u} = [u_x, u_y, \omega_z^c]^{\mathsf{T}} \tag{3.1}$$

The components of the relative deformation can be defined as:

$$\varepsilon_{xx} = \frac{\partial u_x}{\partial x} \tag{3.2}$$

$$\varepsilon_{yy} = \frac{\partial u_y}{\partial y} \tag{3.3}$$

$$\varepsilon_{xy} = \frac{\partial u_y}{\partial x} - \omega_z^c \tag{3.4}$$

$$\varepsilon_{yx} = \frac{\partial u_x}{\partial y} + \omega_z^c \tag{3.5}$$

Micro-curvatures $(\kappa_{xz}, \kappa_{yz})$ enter the kinematics due to the addition of rotational degrees of freedom. They are defined as the gradient of the Cosserat micro-rotations:

$$\kappa_{xz} = \frac{\partial \omega_z^c}{\partial x} \tag{3.6}$$

$$\kappa_{yz} = \frac{\partial \omega_z^c}{\partial y} \tag{3.7}$$

Conjugates of micro-curvatures are the couple stresses (m_{xz}, m_{yz}). They respresent the summation of bending and twisting moments which are transmitted by elements of the material in terms of torque per unit area [49]. The stress-strain relations for Cosserat elasticity for this medium are given as follows [90]:

$$\sigma_{xx} = 2\mu c_1 \varepsilon_{xx} + 2\mu c_2 \varepsilon_{yy} \tag{3.8}$$

$$\sigma_{yy} = 2\mu c_2 \varepsilon_{xx} + 2\mu c_1 \varepsilon_{yy} \tag{3.9}$$

$$\sigma_{(xy)} = \sigma_{(yx)} = 2\mu \varepsilon_{xy} \tag{3.10}$$

$$\sigma_{[xy]} = -\sigma_{[yx]} = -2\mu_c(\omega - \omega_z^c) \tag{3.11}$$

$$m_{xz} = \mathscr{M}\kappa_{xz} \tag{3.12}$$

$$m_{yz} = \mathscr{M}\kappa_{yz} \tag{3.13}$$

where $c_1 = (1-\nu)/(1-2\nu)$ and $c_2 = \nu/(1-2\nu)$. μ is the macroscopic shear modulus. $\sigma_{(.)}$ and $\sigma_{[.]}$ denote the symmetrical and antisymmetrical parts of the shear stresses, respectively. ω is the classical spin which can be computed as:

$$\omega = \frac{1}{2}\left(\frac{\partial u_x}{\partial y} - \frac{\partial u_y}{\partial x}\right) \tag{3.14}$$

μ_c in Eq. (3.11) is an additional material parameter known as Cosserat shear modulus which relates the antisymmetric part of the stress to the relative rotation. $\mathscr{M}$ is a bending modulus with the dimension of force which links the couple stresses to micro-curvatures. An additional material constant therefore needs to be defined for Cosserat elasticity representing an internal length parameter for bending [97]:

$$\ell = \sqrt{\mathscr{M}/\mu} \tag{3.15}$$

ℓ is known as the internal length parameter with the dimension of length. Its order of magnitude represents an important length in the structure under consideration, e.g. grain size in granualr materials. Therefore, two additional independent material constants are needed for Cosserat elasticity, i.e. Cosserat shear modulus and the internal length parameter.
The stress and strain vectors from the classical continuum are extended to accommodate for

micro-curvatures and couple stresses:

$$\boldsymbol{\varepsilon} = [\varepsilon_{xx}, \varepsilon_{yy}, \varepsilon_{zz}, \varepsilon_{xy}, \varepsilon_{yx}, \kappa_{xz}\ell, \kappa_{yz}\ell]^{\mathsf{T}} \tag{3.16}$$

$$\boldsymbol{\sigma} = [\sigma_{xx}, \sigma_{yy}, \sigma_{zz}, \sigma_{xy}, \sigma_{yx}, m_{xz}/\ell, m_{yz}/\ell]^{\mathsf{T}} \tag{3.17}$$

By introducing ℓ in the stress and strain vectors, we can make the terms containing micro-curvatures and couple stresses of the same dimension as the rest of the components.
Figure 3.2 shows the stresses and the couple stresses in an element of a Cosserat medium in 2D. Therefore, the equilibrium equations can be written as:

$$\mathbf{L}^{\mathsf{T}}\boldsymbol{\sigma} + \boldsymbol{b} = \rho\mathbf{g} \tag{3.18}$$

where ρ is the specific density, $\mathbf{g}$ and $\mathbf{b}$ represent gravity acceleration and body forces, respectively. In absence of inertia effects and body forces, Eq. (3.18) could be cast as:

$$\frac{\partial \sigma_{xx}}{\partial x} + \frac{\partial \sigma_{xy}}{\partial y} = 0 \tag{3.19}$$

$$\frac{\partial \sigma_{yx}}{\partial x} + \frac{\partial \sigma_{yy}}{\partial y} = 0 \tag{3.20}$$

The moment equilibrium would be given as:

$$\frac{\partial m_{xz}}{\partial x} + \frac{\partial m_{yz}}{\partial y} - (\sigma_{xy} - \sigma_{yx}) = 0 \tag{3.21}$$

The equilibrium equation shown in Eq. (3.21) results in a generally non-symmetric stress tensor. $\mathbf{L}$ in Eq. (3.18) is given as:

$$\mathbf{L} = \begin{bmatrix} \frac{\partial \cdot}{\partial x} & 0 & 0 \\ 0 & \frac{\partial \cdot}{\partial y} & 0 \\ 0 & 0 & 0 \\ 0 & \frac{\partial \cdot}{\partial x} & -1 \\ \frac{\partial \cdot}{\partial y} & 0 & +1 \\ 0 & 0 & \ell\frac{\partial \cdot}{\partial x} \\ 0 & 0 & \ell\frac{\partial \cdot}{\partial y} \end{bmatrix} \tag{3.22}$$

The plane strain elastic stiffness is defined as:

$$\mathbf{D}^e = \begin{bmatrix} 2\mu c_1 & 2\mu c_2 & 2\mu c_2 & 0 & 0 & 0 & 0 \\ 2\mu c_2 & 2\mu c_1 & 2\mu c_2 & 0 & 0 & 0 & 0 \\ 2\mu c_2 & 2\mu c_2 & 2\mu c_1 & 0 & 0 & 0 & 0 \\ 0 & 0 & 0 & \mu+\mu_c & \mu-\mu_c & 0 & 0 \\ 0 & 0 & 0 & \mu-\mu_c & \mu+\mu_c & 0 & 0 \\ 0 & 0 & 0 & 0 & 0 & 2\mu & 0 \\ 0 & 0 & 0 & 0 & 0 & 0 & 2\mu \end{bmatrix} \tag{3.23}$$

For elastic deformations, stress is given by Eq. (3.24):

$$\boldsymbol{\sigma} = \mathbf{D}^e \boldsymbol{\varepsilon}^e \tag{3.24}$$

where $\boldsymbol{\varepsilon}^e$ is the elastic strain vector.
A non-associated Drucker-Prager type perfect-plasticity model is considered which is appropriate for geo-materials showing friction. The yield criterion is given in Eq. (3.25):

$$f = (3J_2)^{1/2} + \alpha p - k \tag{3.25}$$

Where p is the first stress invariant, known as the hydrostatic pressure and given by Eq. (3.26) and J_2 is the second invariant of deviatoric stresses. α and k represent the friction factor and cohesion constant, respectively. For the Cosserat continuum, a generalised form of J_2 is given in [58] and [60] as in Eq. (3.27):

$$p = \frac{1}{3}(\sigma_{xx} + \sigma_{yy} + \sigma_{zz}) \tag{3.26}$$

$$J_2 = a_1 s_{ij} s_{ij} + a_2 s_{ij} s_{ji} + a_3 m_{ij} m_{ij}/\ell^2 \tag{3.27}$$

where s_{ij} are the component of deviatoric stress tensor. a_1, a_2 and a_3 are additional material parameters. In the absense of couple stresses, $m_{ij} = 0$, we would have $s_{ij} = s_{ji}$ and therefore Eq. (3.27) reduces to:

$$J_2 = (a_1 + a_2) s_{ij} s_{ij} \tag{3.28}$$

Comparing the above with the classical expression for J_2 leads to a constraint as follows:

$$a_1 + a_2 = \frac{1}{2} \tag{3.29}$$

In a compact matrix-vector notation, J_2 can be written as:

$$J_2 = \frac{1}{2}\boldsymbol{\sigma}^{\mathsf{T}}\mathbf{P}\boldsymbol{\sigma} \tag{3.30}$$

Where $\mathbf{P}$ is the projection matrix and defined as:

$$\mathbf{P} = \begin{bmatrix} 2/3 & -1/3 & -1/3 & 0 & 0 & 0 & 0 \\ -1/3 & 2/3 & -1/3 & 0 & 0 & 0 & 0 \\ -1/3 & -1/3 & 2/3 & 0 & 0 & 0 & 0 \\ 0 & 0 & 0 & 2a_1 & 2a_2 & 0 & 0 \\ 0 & 0 & 0 & 2a_2 & 2a_1 & 0 & 0 \\ 0 & 0 & 0 & 0 & 0 & 2a_3 & 0 \\ 0 & 0 & 0 & 0 & 0 & 0 & 2a_3 \end{bmatrix} \tag{3.31}$$

In this paper the values of $a_1 = \frac{1}{4}$, $a_2 = \frac{1}{4}$ and $a_3 = \frac{1}{2}$ are adopted as this will lead to a particularly simple numerical algorithm [25, 26]. The expression for J_2 can then be expanded as:

$$J_2 = \frac{1}{2}[s_{xx}^2 + s_{yy}^2 + s_{zz}^2] + a_1\sigma_{xy}^2 + 2a_2\sigma_{xy}\sigma_{yx} + a_1\sigma_{yx}^2 + a_3[(m_{zx}/\ell)^2 + (m_{zy}/\ell)^2] \tag{3.32}$$

and P simplified to:

$$\mathbf{P} = \begin{bmatrix} 2/3 & -1/3 & -1/3 & 0 & 0 & 0 & 0 \\ -1/3 & 2/3 & -1/3 & 0 & 0 & 0 & 0 \\ -1/3 & -1/3 & 2/3 & 0 & 0 & 0 & 0 \\ 0 & 0 & 0 & \frac{1}{2} & \frac{1}{2} & 0 & 0 \\ 0 & 0 & 0 & \frac{1}{2} & \frac{1}{2} & 0 & 0 \\ 0 & 0 & 0 & 0 & 0 & 1 & 0 \\ 0 & 0 & 0 & 0 & 0 & 0 & 1 \end{bmatrix} \tag{3.33}$$

Eq. (3.25) can now be recast to Eq. (3.34):

$$f = [\frac{3}{2}\boldsymbol{\sigma}^{\mathsf{T}}\mathbf{P}\boldsymbol{\sigma}]^{1/2} + \alpha\boldsymbol{\sigma}^{\mathsf{T}}\boldsymbol{\pi} - k \tag{3.34}$$

where:

$$\boldsymbol{\pi}^{\mathsf{T}} = [1/3, 1/3, 1/3, 0, 0, 0, 0] \tag{3.35}$$

The plastic potential takes a similar form as the yield surface but with a different dilatancy factor, β, as:

$$g = [\frac{3}{2}\boldsymbol{\sigma}^{\mathsf{T}}\mathbf{P}\boldsymbol{\sigma}]^{1/2} + \beta\boldsymbol{\sigma}^{\mathsf{T}}\boldsymbol{\pi} - k \tag{3.36}$$

As in classical plasticity, the flow rule derived from the plastic potential, controls the evolution of plastic strain:

$$\dot{\boldsymbol{\varepsilon}}^{p} = \dot{\lambda}\frac{\partial \boldsymbol{g}}{\partial \boldsymbol{\sigma}} = \dot{\lambda}\boldsymbol{M} \tag{3.37}$$

with the definition:

$$\boldsymbol{M} := \frac{\partial \boldsymbol{g}}{\partial \boldsymbol{\sigma}} = \left[\frac{3\boldsymbol{P}\boldsymbol{\sigma}}{2\sqrt{3/2\boldsymbol{\sigma}^{\mathsf{T}}\boldsymbol{P}\boldsymbol{\sigma}}} + \beta\boldsymbol{\pi}\right] \tag{3.38}$$

$$\dot{\boldsymbol{\varepsilon}}^{p} = \dot{\lambda}\left[\frac{3\boldsymbol{P}\boldsymbol{\sigma}}{2\sqrt{3/2\boldsymbol{\sigma}^{\mathsf{T}}\boldsymbol{P}\boldsymbol{\sigma}}} + \beta\boldsymbol{\pi}\right] \tag{3.39}$$

In analogy with classical plasticity, the rate of the plastic multiplier, $\dot{\lambda}$ is computed from the consistency condition $\dot{f} = 0$. For a perfect plastic model, this can be determined in closed form as:

$$\dot{\lambda} = \frac{\frac{\partial f}{\partial \boldsymbol{\sigma}} : \mathbf{D}^{e} : \dot{\boldsymbol{\varepsilon}}}{\frac{\partial f}{\partial \boldsymbol{\sigma}} : \mathbf{D}^{e} : \frac{\partial g}{\partial \boldsymbol{\sigma}}} = \frac{\boldsymbol{N} : \mathbf{D}^{e} : \dot{\boldsymbol{\varepsilon}}}{\boldsymbol{N} : \mathbf{D}^{e} : \boldsymbol{M}} \tag{3.40}$$

With:

$$\boldsymbol{N} := \frac{\partial f}{\partial \boldsymbol{\sigma}} = \left[\frac{3\boldsymbol{P}\boldsymbol{\sigma}}{2\sqrt{3/2\boldsymbol{\sigma}^{\mathsf{T}}\boldsymbol{P}\boldsymbol{\sigma}}} + \alpha\boldsymbol{\pi}\right] \tag{3.41}$$

3.2.1 Return mapping algorithm

The stress update algorithm considered here is similar to that of classical plasticity. A strain-driven process is considered and the values for stress and state variables are computed at the end of the load step for a given increment in the total strain. The values of the quantities at the previous and current time steps are denoted by $(.)_n$ and $(.)_{n+1}$, respectively. The incremental strain vector can be decomposed into elastic and plastic components under the assumption of small strain theory:

$$\Delta\boldsymbol{\varepsilon}_{n+1} = \Delta\boldsymbol{\varepsilon}^{e}_{n+1} + \Delta\boldsymbol{\varepsilon}^{p}_{n+1} \tag{3.42}$$

Elastic Predictor step

In this stage it is assumed that the material deforms elastically during the load step and no plastic deformation occurs. A trial elastic stress state is then computed as follows:

$$\boldsymbol{\sigma}^{\text{trial}}_{n+1} = \boldsymbol{\sigma}_{n} + \mathbf{D}^{e}\Delta\boldsymbol{\varepsilon}_{n+1} \tag{3.43}$$

Inserting the value of trial stresses in the Eq. (3.25), gives the value for trial yield function as:

$$f_{n+1}^{\text{trial}} = [\frac{3}{2}\boldsymbol{\sigma}_{n+1}^{\text{trial}\,\mathsf{T}}\mathbf{P}\boldsymbol{\sigma}_{n+1}^{\text{trial}}]^{1/2} + \alpha\boldsymbol{\sigma}_{n+1}^{\text{trial}\,\mathsf{T}}\boldsymbol{\pi} - k \tag{3.44}$$

Now if the value of f_{n+1}^{trial} is negative, then the assumption of elastic state was correct, otherwise a plastic corrector step is needed to return the stress state on the yield surface.

Plastic Corrector step

In case the yield criterion is violated, the material has gone through plastic deformation. Eq. (3.40) is integrated using a single point backward Euler method to compute the incremental plastic multiplier and since the vectors $\boldsymbol{N}$ and $\boldsymbol{M}$ are normals to the yield and plastic potential surfaces, respectively, their trial values could be used instead of their updated values. So:

$$\Delta\lambda = \frac{\boldsymbol{N}_{n+1}^{\text{trial}} : \mathbf{D}^e : \Delta\boldsymbol{\varepsilon}_{n+1}}{\boldsymbol{N}_{n+1}^{\text{trial}} : \mathbf{D}^e : \boldsymbol{M}_{n+1}^{\text{trial}}} \tag{3.45}$$

With $\boldsymbol{N}_{n+1}^{\text{trial}}$ and $\boldsymbol{M}_{n+1}^{\text{trial}}$ being computed as:

$$\boldsymbol{N}_{n+1}^{\text{trial}} = \left[\frac{3\boldsymbol{P}\boldsymbol{\sigma}_{n+1}^{\text{trial}}}{2\sqrt{3/2\boldsymbol{\sigma}_{n+1}^{\text{trial}\,\mathsf{T}}\boldsymbol{P}\boldsymbol{\sigma}_{n+1}^{\text{trial}}}} + \alpha\boldsymbol{\pi}\right] \tag{3.46}$$

and

$$\boldsymbol{M}_{n+1}^{\text{trial}} = \left[\frac{3\boldsymbol{P}\boldsymbol{\sigma}_{n+1}^{\text{trial}}}{2\sqrt{3/2\boldsymbol{\sigma}_{n+1}^{\text{trial}\,\mathsf{T}}\boldsymbol{P}\boldsymbol{\sigma}_{n+1}^{\text{trial}}}} + \beta\boldsymbol{\pi}\right] \tag{3.47}$$

The plastic strain rate given by Eq. (3.39) is integrated using a single point backward Euler method resulting in:

$$\Delta\boldsymbol{\varepsilon}_{n+1}^{p} = \Delta\lambda\boldsymbol{M}_{n+1} \tag{3.48}$$

Between the stress and strain increments, a bijective relationship holds:

$$\Delta\boldsymbol{\sigma} = \mathbf{D}^e\Delta\boldsymbol{\varepsilon}_{n+1}^{e} \tag{3.49}$$

By definition the updated value for stress is:

$$\boldsymbol{\sigma}_{n+1} = \boldsymbol{\sigma}_n + \Delta\boldsymbol{\sigma} \tag{3.50}$$

Substitution of Eq. (3.49) into eq. 3.50 leads to:

$$\boldsymbol{\sigma}_{n+1} = \boldsymbol{\sigma}_n + \mathbf{D}^e \Delta\boldsymbol{\varepsilon}^e_{n+1} \tag{3.51}$$

Now substituting Eq. (3.42) into eq. 3.51 gives:

$$\boldsymbol{\sigma}_{n+1} = \boldsymbol{\sigma}_n + \mathbf{D}^e (\Delta\boldsymbol{\varepsilon}_{n+1} - \Delta\boldsymbol{\varepsilon}^p_{n+1}) \tag{3.52}$$

Substituting Eq. (3.52) into Eq. (3.43) gives the updated stresses:

$$\boldsymbol{\sigma}_{n+1} = \boldsymbol{\sigma}^{\text{trial}}_{n+1} - \mathbf{D}^e \Delta\boldsymbol{\varepsilon}^p_{n+1} \tag{3.53}$$

The algorithm for updating the stresses is shown in Algorithm 2. The consistent tangent modulus can also be computed as follows:

$$\dot{\boldsymbol{\sigma}} = \left[\boldsymbol{H} - \frac{\boldsymbol{H}\boldsymbol{M}_{n+1}(\boldsymbol{N}_{n+1})^{\mathsf{T}}\boldsymbol{H}}{(\boldsymbol{N}_{n+1})^{\mathsf{T}}\boldsymbol{H}\boldsymbol{M}_{n+1}} \right] \dot{\boldsymbol{\varepsilon}} \tag{3.54}$$

where:

$$\boldsymbol{H}^{-1} = [\mathbf{D}^e]^{-1} + \Delta\lambda \sqrt{\frac{3}{2}} \frac{\boldsymbol{\sigma}^{\mathsf{T}}_{n+1}\boldsymbol{P}\boldsymbol{\sigma}_{n+1}\boldsymbol{P} - \boldsymbol{P}\boldsymbol{\sigma}_{n+1}\boldsymbol{\sigma}^{\mathsf{T}}_{n+1}\boldsymbol{P}}{\sqrt{\boldsymbol{\sigma}^{\mathsf{T}}_{n+1}\boldsymbol{P}\boldsymbol{\sigma}_{n+1}}} \tag{3.55}$$

Algorithm 2: Stress update algorithm for the Drucker-Prager plasticity model

1. Given the database and history variables ε_n^p at time t_n.
2. Advance the strain to ε_{n+1} at time t_{n+1}
   $\Delta\varepsilon_{n+1} = \varepsilon_{n+1} - \varepsilon_n$
3. Elastic predictor step
   $\boldsymbol{\sigma}_{n+1}^{\text{trial}} = \boldsymbol{\sigma}_n + \mathbf{D}^e \Delta\boldsymbol{\varepsilon}_{n+1}$
   - Compute trial yield function according to Eq. (3.44)
   - Check for plastic loading
     IF ($f_{n+1}^{\text{trial}} < 0$) THEN
     The assumption for elastic step is valid
     set $(.)_{n+1} := (.)_{n+1}^{\text{trial}}$
     GOTO 5

   ENDIF
4. Plastic corrector step
   - Compute incremental plastic multiplier according to Eq. (3.45)
   - Compute incremental plastic strain according to Eq. (3.48)
   - Update the stresses according to Eq. (3.53)
   - Update history variables (plastic strains)
     $\boldsymbol{\varepsilon}_{n+1}^p = \boldsymbol{\varepsilon}_n^p + \Delta\boldsymbol{\varepsilon}_{n+1}^p$
5. EXIT

Chapter 4

Mesh-objective numerical simulation of non-associated plasticity problems using Cosserat continuum model

4.1 Introduction

In this chapter, two aspects of mesh dependency of the numerical analysis, namely the dependency on the discretization size and orientation, in classical non-associated plasticity are demonstrated using two localisation problems. First, a 1D shear layer problem in pure shear is taken for an in-depth analysis of mesh size dependency. It will be examined in detail, analytically and numerically, regarding the occurrence of mesh dependence and structural softening caused by non-associated plastic flow. The shear layer is then re-analysed with the enriched Cosserat continuum model, and the results are shown to be mesh objective, yet still exhibiting structural softening.

Second, a numerical example of a biaxial test under compression is considered. Numerical simulations show the dependence of the deformation on the spatial discretisation both in terms of its density and of the direction of the mesh lines. The Cosserat continuum model is then used, which results in objectivity with respect to the mesh size as well as the mesh orientation.

4.2 Analysis of a shear layer [1]

To investigate the structural softening and mesh dependence encountered in the shear-band simulation of the biaxial test in more detail, we consider the simpler case of a shear layer under plane-strain conditions, which is infinitely long in the horizontal x-direction, as shown in Figure 4.1. The discretised shear layer is amenable to an analytical solution, which we will compare with a numerical simulation for different mesh densities.

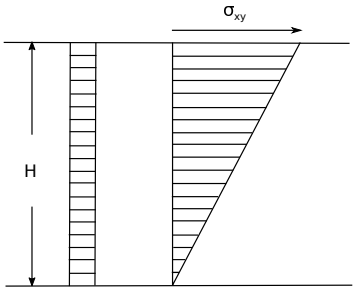

Fig. 4.1 An infinitely long shear layer

4.2.1 Analytical solution

We assume that the shear layer is sub-divided into m elements (constant strain). One element has a marginally lower shear strength than the other $m-1$ elements and will therefore plasticise, while the remaining elements unload. For this element, the shear strain can be decomposed as:

$$\gamma = \gamma^e + \gamma^p \tag{4.1}$$

With τ the shear stress and μ the shear modulus, so that $\gamma^e = \tau/\mu$, we can rewrite Eq. (4.1) as:

$$\gamma = \frac{\tau}{\mu} + \gamma^p \tag{4.2}$$

We adopt a Drucker-Prager yield function,

$$f = \sqrt{3J_2} + \alpha^* p - k^* \tag{4.3}$$

[1] Based on: Sabet, S. A. and de Borst, R. (2019). Structural softening, mesh dependence, and regularisation in non-associated plastic. *International Journal for Numerical and Analytical Methods in Geomechanics*, 43(13):2170-2183

with the material parameters α^* and k^* related to the cohesion c and the angle of internal friction, ϕ. Considering plane-strain conditions, Eq. (4.3) reduces to:

$$f = \tau + \alpha p - k \tag{4.4}$$

under pure shear loading, where

$$\alpha = \frac{2\sqrt{3}\sin\phi}{3-\sin\phi} \quad , \quad k = \frac{2\sqrt{3}c\cos\phi}{3-\sin\phi} \tag{4.5}$$

In a standard manner, a plastic potential function is introduced:

$$g = \tau + \beta p \tag{4.6}$$

where β is related to the dilatancy angle ψ similar to the relation between α and ϕ in Eq. (4.5). The plastic shear and volumetric strain rates then directly follow as:

$$\begin{cases} \dot{\gamma}^p = \dot{\lambda}\frac{\partial g}{\partial \tau} = \dot{\lambda} \\ \dot{\varepsilon}_v^p = \dot{\lambda}\frac{\partial g}{\partial p} = \dot{\lambda}\beta \end{cases} \tag{4.7}$$

which results in the dilatancy relation:

$$\dot{\gamma}^p = \frac{\dot{\varepsilon}_v^p}{\beta} \tag{4.8}$$

and for proportional loading:

$$\gamma^p = \frac{\varepsilon_v^p}{\beta} \tag{4.9}$$

With the additive decomposition for the volumetric strain:

$$\varepsilon_v = \varepsilon_v^e + \varepsilon_v^p \tag{4.10}$$

Eq. (4.8) becomes:

$$\gamma^p = \frac{\varepsilon_v - \varepsilon_v^e}{\beta} \tag{4.11}$$

Since $\varepsilon_v^e = p/\kappa$, with κ the bulk modulus, we can rewrite Eq. (4.11) as:

$$\gamma^p = \frac{\varepsilon_v}{\beta} - \frac{p}{\beta\kappa} \tag{4.12}$$

and Eq. (4.2) becomes:

$$\gamma = \frac{\tau}{\mu} - \frac{p}{\beta\kappa} + \frac{\varepsilon_v}{\beta} \tag{4.13}$$

Since the yield condition must hold during progressive yielding, i.e. $f = 0$, we have from Eq. (4.4):

$$p = \frac{k - \tau}{\alpha} \tag{4.14}$$

and Eq. (4.13) becomes:

$$\gamma = \frac{\tau}{\mu} + \frac{\tau - k}{\alpha\beta\kappa} + \frac{\varepsilon_v}{\beta} \tag{4.15}$$

We assume that all m elements have an equal length, $\mathscr{L}$. For the total height of the layer we thus have $H = m\mathscr{L}$. There are two possibilities for ε_v.

Case I: We assume that $\varepsilon_v = 0$ on a pointwise basis, in this case for each (constant strain) element. Numerically, this can be realised by preventing each element from displacing vertically. Eq. (4.15) then reduces to:

$$\gamma = \frac{\tau}{\mu} + \frac{\tau - k}{\alpha\beta\kappa} \tag{4.16}$$

Noting that only in the weakened element we have elasto-plastic deformations, and the remaining $m - 1$ elements feature only elastic strains, the horizontal displacement at the top of the layer reads:

$$u = \gamma\mathscr{L} + (m-1)\mathscr{L}\frac{\tau}{\mu} \tag{4.17}$$

or using Eq. (4.16):

$$u = m\mathscr{L}\frac{\tau}{\mu} + \mathscr{L}\frac{\tau - k}{\alpha\beta\kappa} \tag{4.18}$$

Hence, the average shear strain over the layer becomes:

$$\bar{\gamma} = \frac{u}{H} = \frac{\tau}{\mu} + \frac{\tau - k}{m\alpha\beta\kappa} \tag{4.19}$$

Eq. (4.19) shows that there is a clear mesh dependence since, when increasing m, the response becomes more brittle. When $\tau \downarrow 0$, we have an inverse dependence on the numbers of elements:

$$\lim_{\tau \to 0} \bar{\gamma} = -\frac{k}{m\alpha\beta\kappa} \tag{4.20}$$

We note that $\alpha \geq 0$ and $\kappa > 0$, but that for plastic contraction $\beta < 0$. For $\tau \downarrow 0$, we therefore have $\bar{\gamma} > 0$.

Case II: The condition of incompressibility $\varepsilon_v = 0$ is not imposed pointwise, but over the entire shear layer. This implies that part of the plastic expansion/contraction in the failing element can be compensated by elastic volumetric strains in the other elements. Numerically, this condition can be simulated by only prescribing roller boundary conditions at the top of the layer together with linear dependence (master-slave) relations to ensure that nodes on the same horizontal line displace the same amount. It is noted that when imposing this condition, the other $(m-1)$ elements may satisfy the yield condition at some point.

Let the incremental shear strain be denoted by $\Delta\gamma$. Then, the additional horizontal displacements at the top of the layer is

$$\Delta u = \Delta\gamma^w \mathscr{L} + (m-1)\Delta\gamma^l \mathscr{L} \tag{4.21}$$

where the superscripts w and l denote the weak element and the remainder of the layer, respectively. Substitution of Eq. (4.2) then gives:

$$\frac{\Delta u}{\mathscr{L}} = \frac{\Delta\tau}{\mu} + (\Delta\gamma^p)^w + (m-1)\left(\frac{\Delta\tau}{\mu} + (\Delta\gamma^p)^l\right) \tag{4.22}$$

Use of the dilatancy relation, Eq. (4.9), subsequently gives:

$$\frac{\Delta u}{\mathscr{L}} = m\frac{\Delta\tau}{\mu} + \frac{1}{\beta}\left((\Delta\varepsilon_v^p)^w + (m-1)(\Delta\varepsilon_v^p)^l\right) \tag{4.23}$$

Exploiting the additive decomposition of the strain into an elastic and a plastic component, and considering that the shear layer deforms isochorically, we obtain:

$$\frac{\Delta u}{\mathscr{L}} = m\frac{\Delta\tau}{\mu} - \frac{1}{\beta}\left((\Delta\varepsilon_v^e)^w + (m-1)(\Delta\varepsilon_v^e)^l\right) \tag{4.24}$$

Since the stresses are on the yield surface, the consistency condition holds for a finite increment:

$$\Delta p = -\frac{\Delta\tau}{\alpha} \tag{4.25}$$

so that:

$$(\Delta\varepsilon_v^e)^w = (\Delta\varepsilon_v^e)^l = \frac{\Delta p}{\kappa} = -\frac{\Delta\tau}{\alpha\kappa} \tag{4.26}$$

Substitution into Eq. (4.24) then yields:

$$\Delta\bar{\gamma} = \frac{\Delta u}{H} = \frac{\Delta\tau}{\mu} + \frac{\Delta\tau}{\alpha\beta\kappa} \tag{4.27}$$

giving a slope:

$$\frac{d\bar{\gamma}}{d\tau} = \frac{1}{\mu} + \frac{1}{\alpha\beta\kappa} \tag{4.28}$$

Physically, α, μ and κ must be positive. However, $\beta < 0$ for plastic contraction, and, depending on the precise values of α, β, μ and κ, we have $\frac{d\bar{\gamma}}{d\tau} < 0$, leading to structural softening. However, since m has dropped out of the expression, there is no mesh dependence under the current assumption.

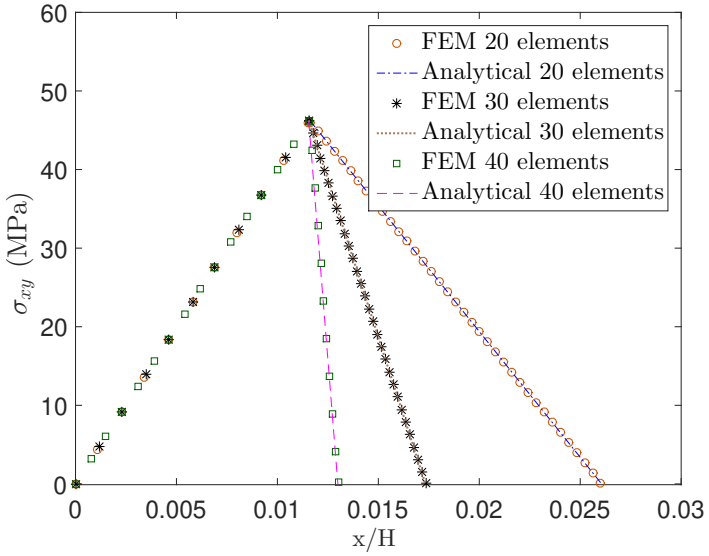

Fig. 4.2 Load-displacement curves for Case I of the infinitely long shear layer

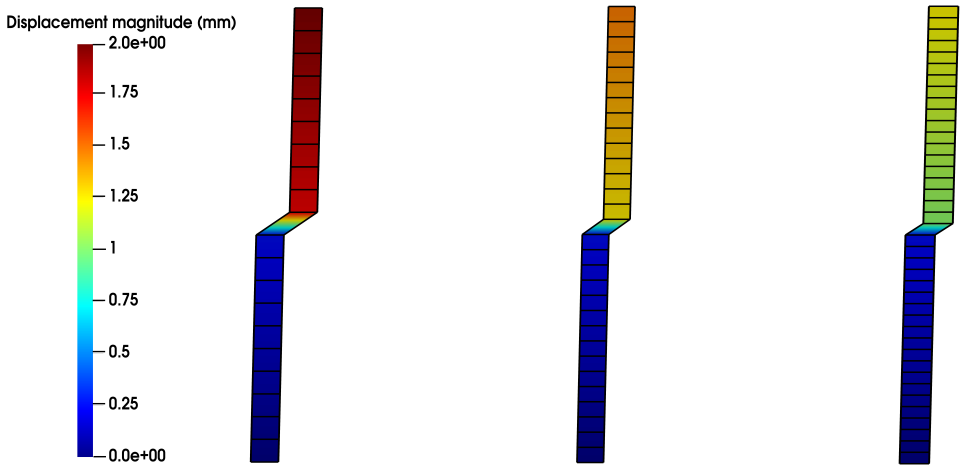

Fig. 4.3 Deformed model for Case I, at $\tau = 20$ MPa, using a standard Drucker-Prager model

4.2.2 Numerical classical plasticity solution

We first consider Case I, and analyse a layer with a height $H = 100$ mm. The material parameters have been taken as Young's modulus $E = 10000$ MPa and Poisson's ratio $\nu = 0.25$, while for the plasticity the following values have been used: $\alpha = 0.2$, $\beta = -0.2$ and $k = 100$ MPa, with the latter parameter reduced by 20% for the weaker element. Three mesh densities have been used, with 20, 30 and 40 linear quadrilateral elements, respectively. A standard Gauss integration scheme is used. The load-displacement curves have been plotted in Figure 4.2 along with the corresponding analytical solutions, cf. Eq. (4.19). The numerical results fully coincide with the analytical solution.

For all discretisations a clear structural softening is observed just after reaching the peak load. Moreover, a mesh dependence is observed, i.e. for finer meshes the descending branch of the post-peak load-displacement curve becomes steeper, which is also corroborated by the analytical results. It is also apparent that localisation is confined to a single element (layer), see Figure 4.3, which shows the deformed contours of the shear layer beyond peak load at $\tau = 20$ MPa. We next consider case II, with again three different discretisations, but

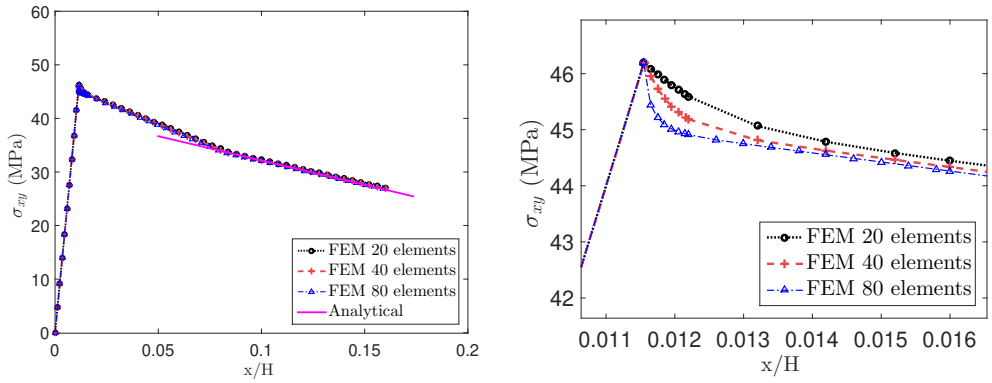

(a) Full diagram

(b) Zoom post peak

Fig. 4.4 Load vs displacement for Case II of the infinitely long shear layer

now with 20, 40 and 80 elements, respectively. As with Case I, there is a clear structural softening, see Figure 4.4. However, the numerical and analytical solutions only match after progressive deformations, and then indeed do not exhibit any mesh dependence, as predicted by the analytical solution of Eq. (4.28). The discrepancy between the analytical solution and the numerical results is due to the fact that the assumption is violated that there are no plastic strains outside the weaker element. Because of the occurrence of plastic straining outside the weak element right after the peak load the numerical results there also become slightly mesh dependent, as shown in the zoom. At progressive overall displacements the plastic zone again becomes confined to the weaker element and the assumption underlying

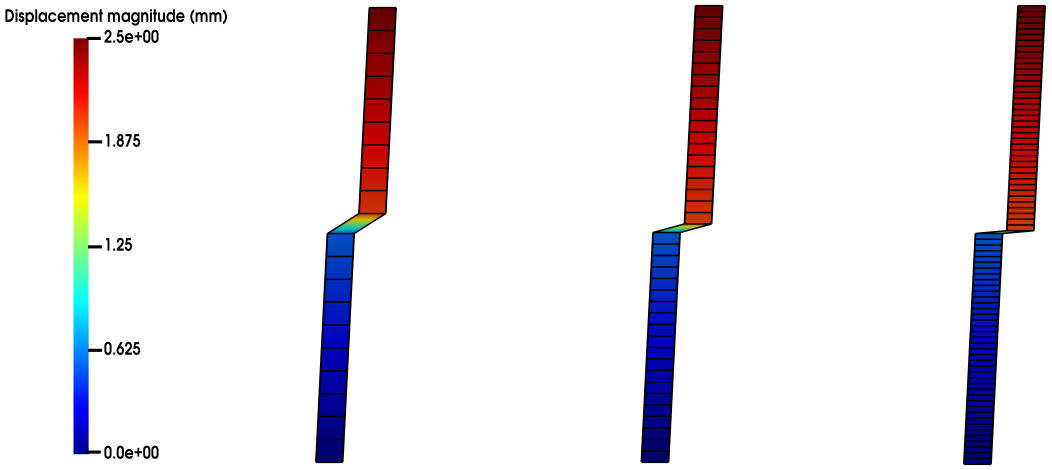

Fig. 4.5 Deformed contours for Case II, at $\tau = 43$ MPa using a standard Drucker-Prager model

the analytical solution is satisfied. Figure 4.5 shows the deformed contours at a residual shear stress level $\tau = 43$ MPa. As with the previous case, localisation is confined to a single element, irrespective of the number of elements used to model the shear layer.

4.2.3 Numerical Cosserat plasticity solution

The shear layer is re-analysed here using the Cosserat Drucker-Prager plasticity model, as described in chapter 3. The material parameters used for the Cosserat Drucker-Prager plasticity model have been kept the same as those used in the classical Drucker-Prager model. Regarding the two additional parameters needed for planar deformations, we have assumed that $\mu_c = 2000$ MPa, while two values have been adopted for the characteristic length, namely $\ell = 2$ mm and $\ell = 5$ mm. The results of an analysis of the shear layer for Case I, but now using the Cosserat continuum, are discussed below.

The load-displacement curves in Figures 4.6a and 4.6b show that the results are now mesh independent, in the sense that they converge to a unique, physically realistic solution upon mesh refinement, which is different from the computations for the standard Drucker-Prager non-associated plasticity model. Figure 4.7 also shows the convergence of stress at top of the shear layer with respect to the element size in logarithmic scale. We emphasise that the introduction of the internal length scale ℓ, however, does not remove structural softening. Indeed, the internal length scale not only controls the width of the localisation zone, cf. Figures 4.8 and 4.9, but also the slope of the load-deformation curve. For a lower value of ℓ a more brittle post-peak behaviour occurs.

Case II was also re-analysed using the Cosserat continuum, and showed similar results as the computations for Case I. While the analysis of mesh dependence is not relevant now, the results continue to exhibit structural softening for the chosen set of material parameters. And like for Case I, but different from the results for the classical continuum, a width of the localisation zone appears which is independent of the discretisation for sufficiently dense meshes.

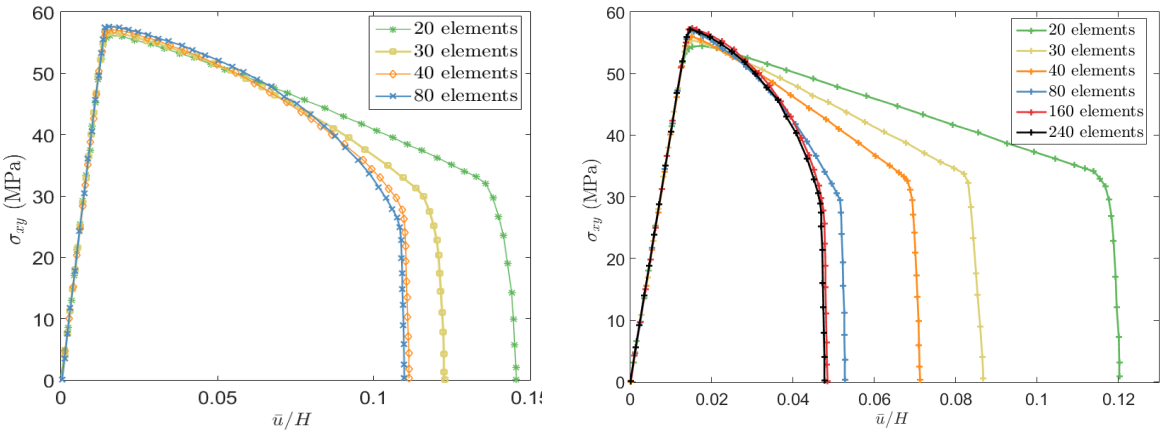

(a) $l = 5$ mm (b) $l = 2$ mm

Fig. 4.6 Load-displacement curves for Case I, using a Cosserat Drucker-Prager model

4.3 Analysis of a biaxial test [2]

4.3.1 Model set-up

A compression biaxial test is considered in order to investigate the influence of the mesh density and the mesh orientation during shear banding. The geometry and the boundary conditions are shown in Figure 4.10. The dimensions of the specimen are $L = 20$ cm and $W = 10$ cm, respectively. A compressive stress field results from a smooth, rigid platen being moved downwards uniformly at the top of the specimen. A non-associated elastic-ideally plastic Drucker-Prager type material model is considered for this problem. The parameters used are summarised in table 4.1. Eq. (2.94) have been used to compute α and β.

[2]Based on: Sabet, S. A. and de Borst, R. (2019). Mesh bias and shear band inclination in standard and non-standard continua. *Archive of Applied Mechanics*, 89(12): 2577-2590.

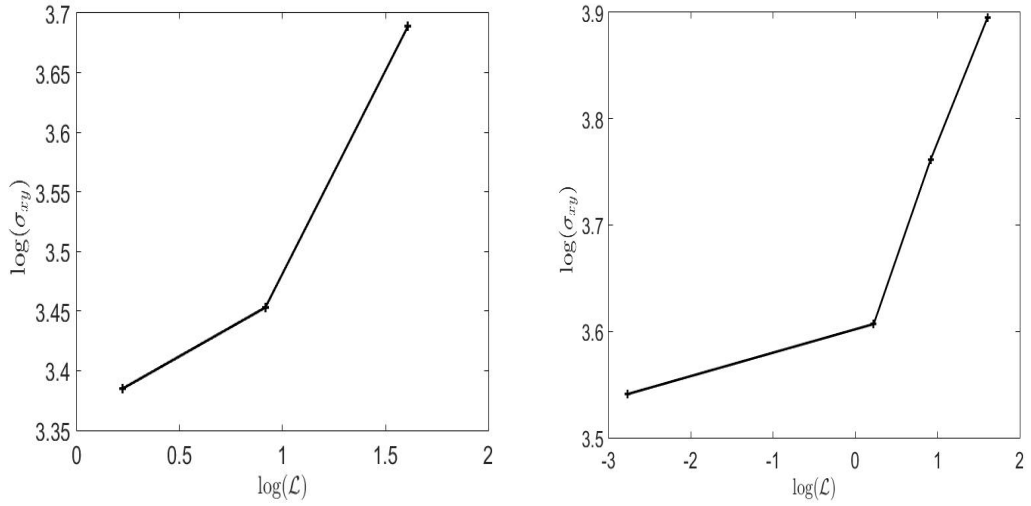

(a) $l = 5$ mm (b) $l = 2$ mm

Fig. 4.7 Convergence of stress at top of the shear layer *vs* element size for Case I, using a Cosserat plasticity, a) at $\bar{u}/H = 0.104$ and b) at $\bar{u}/H = 0.045$

Table 4.1 Parameters used for the Drucker-Prager model in Figure 4.10

Parameter	Symbol	Value
Young's modulus	E	100 KPa
Poisson's ratio	ν	0.25
Internal friction angle	ϕ	25°
Dilation angle	ψ	5°
Cohesion	c	0.06 KPa
Internal friction coefficient	α	0.984
Dilatancy factor	β	0.18

4.3.2 Mesh arrangements

In the numerical analyses two different mesh arrangements, model A and model B, have been used, each composed of quadratic triangular elements in a crossed lay-out. Use of these elements avoids the problem of volumetric locking and makes it more convenient to study directional mesh bias. A standard Gauss integration scheme is used. Model A has been analysed for three different mesh sizes, 4×6, 8×12 and 16×24 elements. In model A, the elements have been arranged such that the angle of the element boundaries is at 53.1°, which is close to the expected direction of shear banding according to the Arthur solution, i.e. 52.5° for the chosen parameter set, see Section 4.3.1. In model B, the diagonals of the mesh are

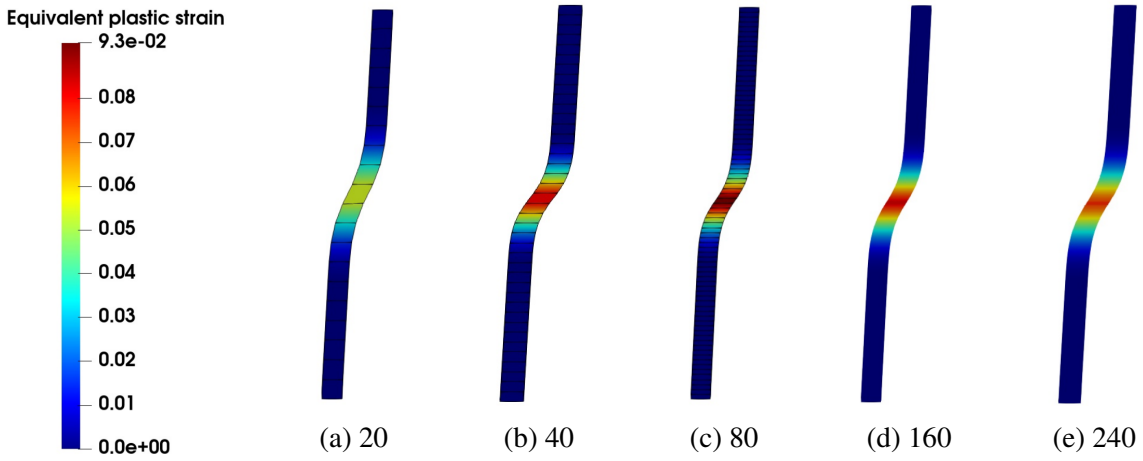

Fig. 4.8 Deformed contours for Case I, with $\ell = 2$ mm, at $u = 3.1$ mm, using Cosserat Drucker-Prager model

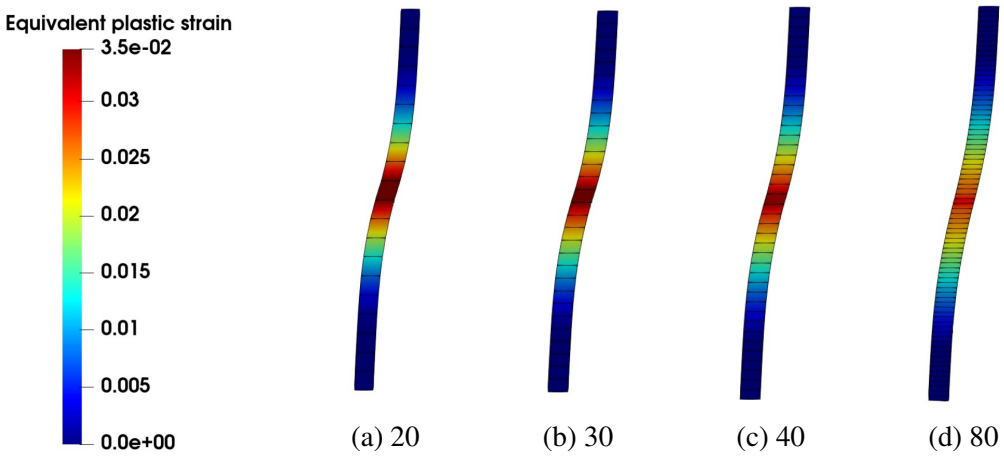

Fig. 4.9 Deformed contours for Case I, with $\ell = 5$ mm, at $u = 3.1$ mm, using a Cosserat Drucker-Prager model

very different at a value of 69.4^{o}, see Figure 4.11. Three different discretisation levels have also been considered now, 8×6, 16×12 and 32×24.

To induce a non-homogeneous stress field and hence to trigger localisation, an imperfect element with a 16.7% reduction in the cohesive strength has been inserted at the left boundary, just above the centre line in both models.

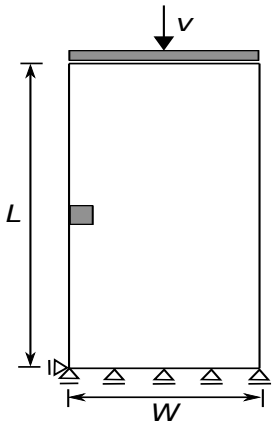

Fig. 4.10 Geometry with boundary conditions and imperfection

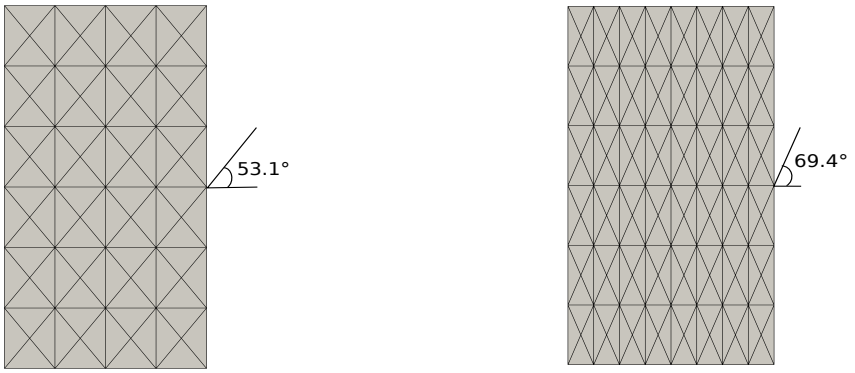

(a) Model A (b) Model B

Fig. 4.11 Two discretisations with different mesh directions

4.3.3 Shear banding in a standard elasto-plastic continuum

Sensitivity to mesh size

Localisation zones develop starting from the imperfection and continue to grow until a peak in the load-displacement curve, Figure 4.12, has been reached. At this point loss of uniqueness of the solution occurs and the boundary-value problem becomes ill-posed. A post-peak structural softening is observed for all discretisations of model A. The slope of the softening becomes steeper upon mesh refinement. It is emphasised that the structural softening is here purely a consequence of the use of a non-associated flow rule, and has been observed before in computations [24] and has been analysed in depth [50, 88].

Since the boundary-value problem becomes ill-posed at this point obtaining a converged solution becomes difficult. Indeed, for the fine mesh of model A divergence occurs shortly after the peak load even for extremely small load steps. A possible reason is that snap-back

behaviour may occur which cannot be resolved under displacement control. From Figure 4.13 it can be seen that in model A a highly localised shear band is formed and that the size of the shear band is dominated by the mesh size. The shear band is confined to a single band of elements. If the element size approaches zero, the shear band width would also becomes zero and the load-displacement curve would double back on the loading branch, resulting in a physically meaningless solution with zero energy dissipation [28].

The results for model B also show post-peak structural softening, but only for the finer discretisations (16×12 and 32×24). A poor convergence behaviour with severe oscillations is observed upon mesh refinement. Indeed, for the finest mesh the solution procedure breaks down after reaching a plateau. The residual load level, i.e. the load level which is reached after structural softening, is slightly higher in model B than in model A. A shear band also forms in model B, but is considerably more diffuse than in model A, see Figure 4.14.

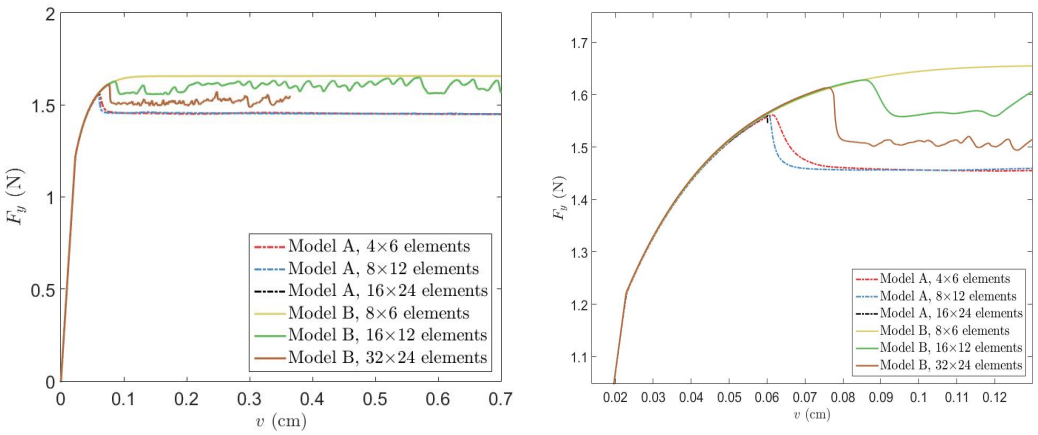

(a) Full curve (b) Zoom post-peak

Fig. 4.12 Load-displacement curves for model A and B using a standard Drucker-Prager model

Sensitivity to mesh alignment

Figure 4.15 shows the bias of the initial element arrangement on the shear band. In model A shear band formation occurs along the edges of the elements, and therefore, the orientation is dominated by the mesh diagonals, i.e. at $\vartheta = 53^{\circ}$, which is close to the Arthur solution, $\vartheta = 45^{\circ} + (\phi + \psi)/4 = 52.5^{\circ}$ [5]. It is emphasised that this correct inclination has been helped by the initial mesh lay-out, with diagionals at $\vartheta = 53.1^{\circ}$, cf. Section 4.3.1. For model B the angle at which the shear band forms is also influenced by the mesh orientation, and

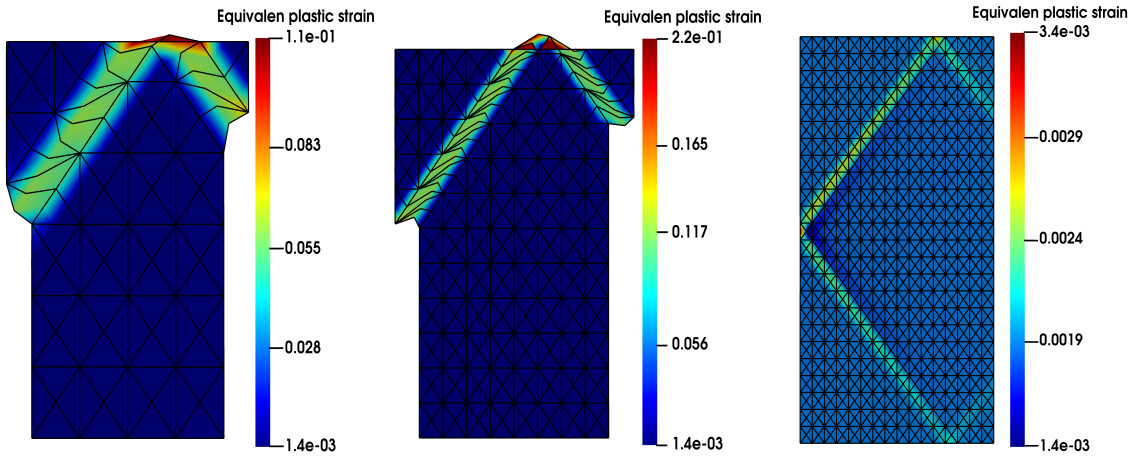

(a) 4×6 elements (b) 8×12 elements (c) 16×24 elements

Fig. 4.13 Equivalent plastic strain for model A, a) and b) at $v = 0.2$ cm, c) shortly before the iterative solution fails, at $v = 0.06$ cm

shear bands form at $\vartheta = 60^{\circ}$ degrees. This difference shows how the mesh orientation can bias the solution for ill-posed boundary value problems.

4.3.4 Computations with Cosserat elasto-plasticity model

The biaxial test considered in Section 4.3.1 has bee re-analysed using Cosserat elasto-plasticity. The set-up and material parameters are as before. Two additional material parameters, $\mu_c = 20$ kPa and a characteristic length $\ell = 1$ mm have been adopted for the Cosserat model. The parameter values have been chosen such that they properly bring out the regularising effect without requiring an overly dense discretisation. A procedure to determine the additional material parameters in a Cosserat continuum has been described in [40].
Model A has been analysed with four different levels of mesh refinement, 4×6, 8×12, 16×24, 32×48 elements and model B has been analysed for the same discretisations as before.

Objectivity with respect to the mesh density

The load-displacement curves for models A and B are shown in Figures 4.16a and 4.16b, respectively. They show that in both models the results converge to a unique solution upon refinement of the discretisation, which is in contrast to the results for standard non-associated Drucker-Prager plasticity. For a sufficient refinement level, the width of the shear bands is not affected by the mesh size, neither in model A, nor in model B. Figure 4.17 also shows that the solutions of models A and B then agree well. For the assumed characteristic length scale,

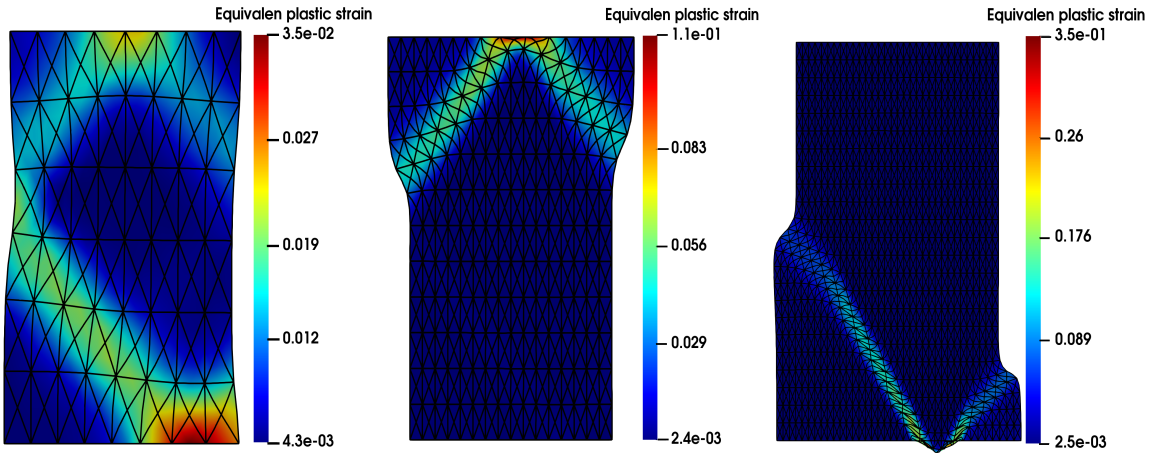

(a) 8×6 elements (b) 16×12 elements (c) 32×24 elements

Fig. 4.14 Equivalent plastic strain for model B, at $v = 0.2$ cm, using a standard Drucker-Prager model

a mild structural softening occurs, but this is no longer mesh-dependent after a converged solution has been obtained. The equivalent plastic strain contours, see Figures 4.18 and 4.19, also show that strains are not localised over a single layer of elements, but over a shear band with a finite width of approximately 16 mm, which makes that the ratio of the shear band width over the internal length scale is in the range of established theoretical values [63] and experimental observations [104].

As it has been mentioned here and in Section 4.2.3, using Cosserat continuum model does not eliminate structural softening. This has been demonstrated in Figure 4.20 where a more pronounced structural softening is seen for the finest descritisation of model B. The same parameters have been used for this simulation except the friction coefficient and dilation factor which are considered as $\alpha = 1.2$ and $\beta = 0$.

Objectivity with respect to the orientation of the mesh lines

Comparing Figures 4.18 and 4.19 reveals a very similar shear band pattern and orientation angle for both models after sufficient refinement. Upon mesh refinement each model converges to a unique solution, and there is a very good agreement in terms of the inclination angle of the shear band. The observed shear band patterning is characteristic for the use of a Cosserat continuum model.

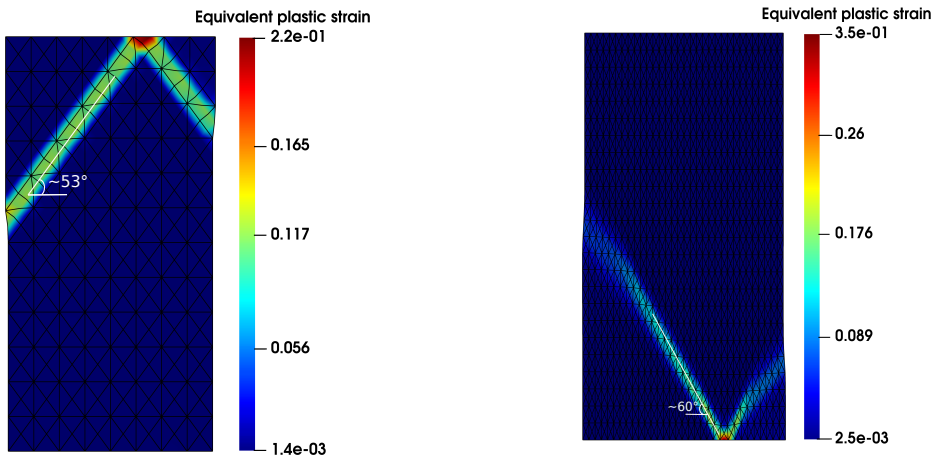

(a) Model A (b) Model B

Fig. 4.15 Shear band orientation in model A *vs* model B

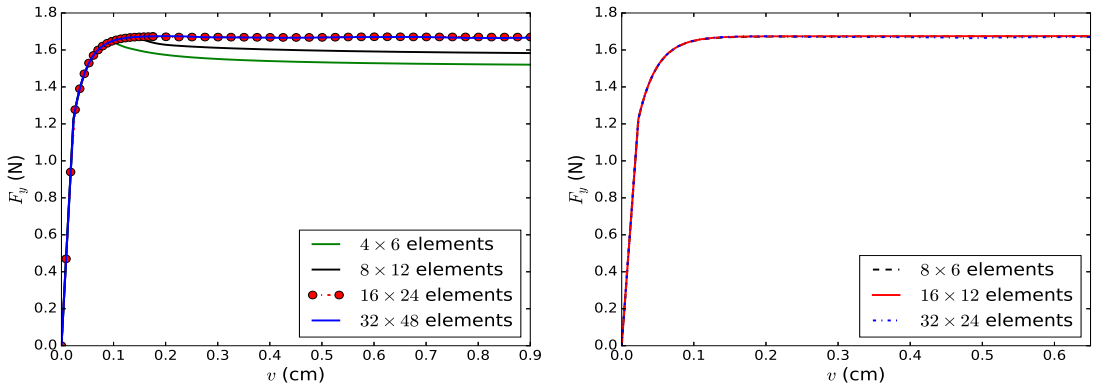

(a) Model A (b) Model B

Fig. 4.16 Load-displacement curves for biaxial test using Cosserat plasticity

Shear-band orientation

The shear bands form at approximately $\vartheta = 48^{\circ}$ both in model A and in model B when using Cosserat Drucker-Prager plasticity, as shown in Figure 4.21. This is different from the shear band inclination angles from classical bifurcation theory, which rather suggest $\vartheta = 52.5^{\circ}$. In fact, they closer match the Roscoe solution ($\vartheta = 45^{\circ} + \psi/2 = 47.5^{\circ}$). This suggests that the introduction of an internal length scale to represent the grain size can result in a reproduction of the experimental observation that the inclination angle depends on the grain size [33, 38].

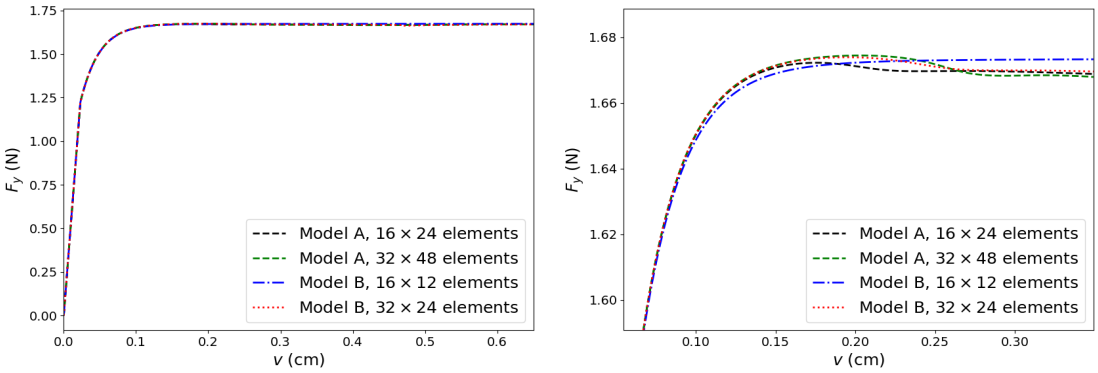

(a) Full curve (b) Zoom post-peak

Fig. 4.17 Comparison of load-displacement curves using Cosserat plasticity

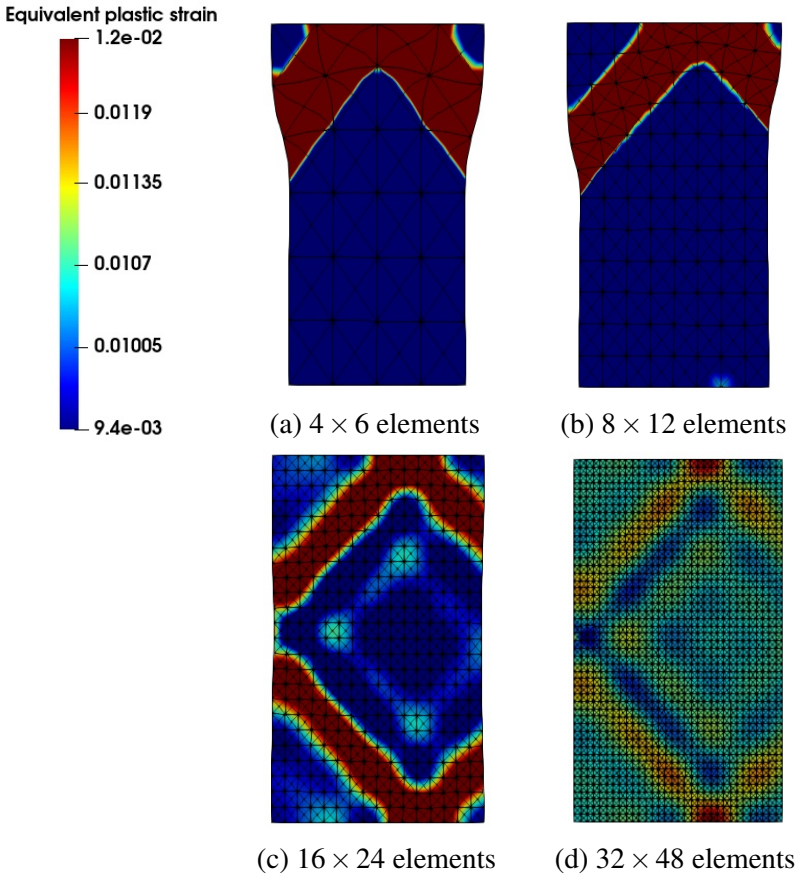

(a) 4×6 elements (b) 8×12 elements

(c) 16×24 elements (d) 32×48 elements

Fig. 4.18 Equivalent plastic strain for model A, at $v = 0.2$ cm, using Cosserat Drucker-Prager plasticity

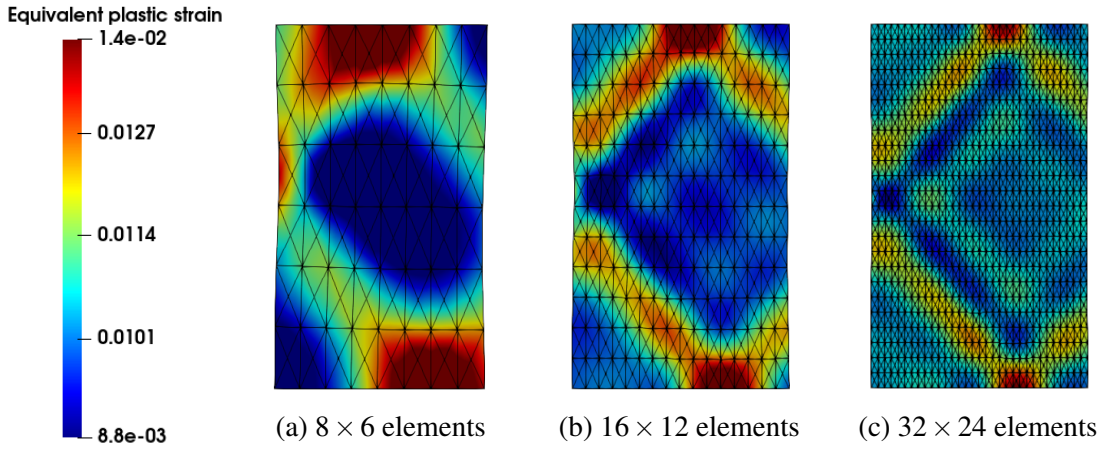

(a) 8×6 elements (b) 16×12 elements (c) 32×24 elements

Fig. 4.19 Equivalent plastic strain for model B, at $v = 0.2$ cm, using Cosserat Drucker-Prager plasticity

4.4 Concluding remarks

The structural softening and mesh dependence which have been encountered in the preceding examples are due to a loss of uniqueness of the solution of the governing set of partial differential equations. In this chapter, it has been demonstrated how a standard continuum suffers from a loss of uniqueness of the solution at the onset of localisation, which leads to mesh dependence both in terms of the size and the orientation. As has been stated in chapter 1, this can be prevented by using a non-Boltzmann continuum model or by introducing rate dependence. Herein, we have examined whether a Cosserat continuum model is also effective in preventing loss of uniqueness of the solution and ensuing mesh size and alignment dependency for non-associated plasticity. The results confirm that mesh-objective results can be obtained in the numerical simulations using a Cosserat continuum model and that it can be an effective localisation limiter for non-associated flow as well [86–88].

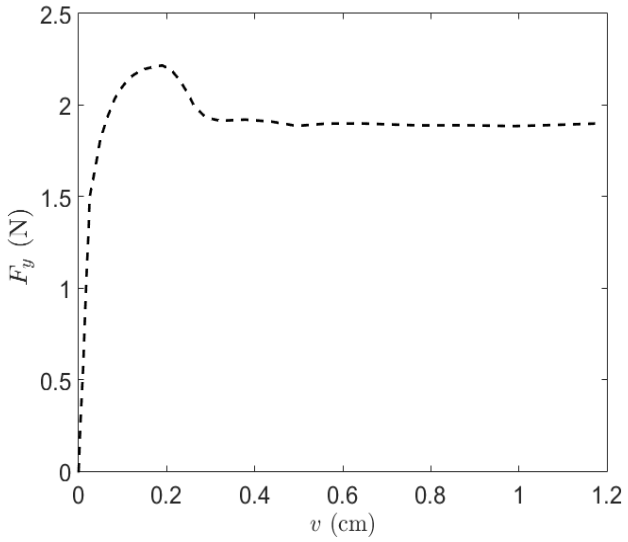

Fig. 4.20 Pronounced structural softening for model B using Cosserat plasticity for finest mesh(32×24) with $\alpha = 1.2$ and $\beta = 0$

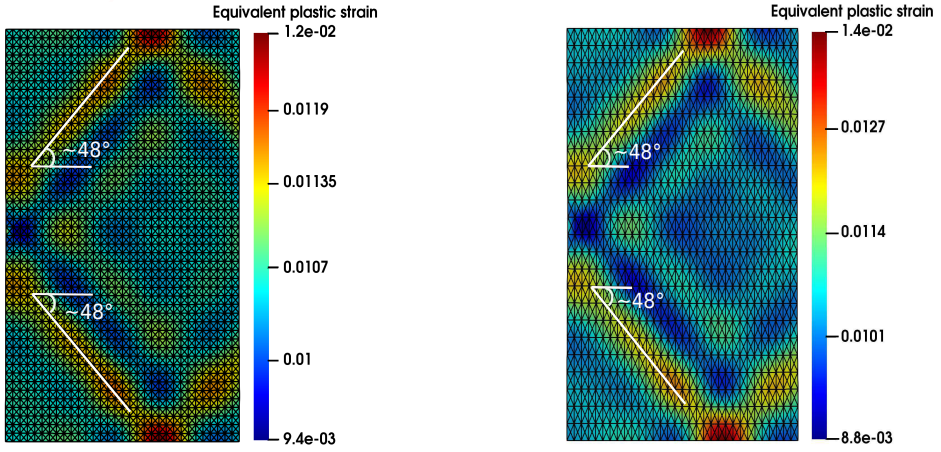

(a) Model A (b) Model B

Fig. 4.21 Shear band angles for both models (A and B) using Cosserat plasticity

Chapter 5

Conclusions and outlook

5.1 Conclusions [1], [2]

Numerical simulations using plasticity models with a non-associated flow rule embedded in a classical (Boltzmann) continuum show that structural softening can occur in spite of the fact that no explicit strain softening is applied to the cohesion or to the angle of internal friction [24, 50]. Moreover, a dependence of the solution on the discretisation emerges. This mesh dependence not only relates to the mesh density, but also to the orientation of the mesh lines, as shear bands tend to follow the mesh lines. However, the extent depends on the precise boundary value problem. In most cases the mesh dependence only manifests itself for a limited deformation range beyond the peak load, and mesh effects level out on progressive deformation, and a unique residual load is usually attained, independent of the discretisation.

The underlying reason of the mesh sensitivity is the loss of well-posedness, which occurs at a certain stage of the loading process when using a non-associated flow rule, and occurs even though strain softening is not included explicitly in the constitutive model, with the displacement gradients remaining infinitesimal [53, 84, 65, 108].

The Cosserat continuum can be exploited to remedy this deficiency [63, 91, 2], as it introduces an internal length scale. Indeed, numerical simulations show that the localisation zone then remains finite, and that load-displacements curves converge to a unique solution upon mesh refinement. The slope of the post-peak load-displacement curve and the width of the localisation zone are then set by the internal length scale. It is emphasised though, that structural softening is not removed by the regularisation, as has been demonstrated numeri-

[1] Partly based on: Sabet, S. A. and de Borst, R. (2019). Structural softening, mesh dependence, and regularisation in non-associated plastic. *International Journal for Numerical and Analytical Methods in Geomechanics*, 43(13):2170-2183

[2] Partly based on:Sabet, S. A. and de Borst, R. (2019). Mesh bias and shear band inclination in standard and non-standard continua. *Archive of Applied Mechanics*, 89(12): 2577-2590.

cally. Furthermore, computations become independent of the orientation of discretisation, and shear bands are no longer biased by the orientation of the mesh lines.

The use of an enhanced continuum to prevent loss of well-posedness of quasi-static calculations not only has implications for mesh sensitivity. It also has consequences for computability as the global convergence behaviour of the non-linear solver can be improved dramatically. Computations with non-associated flow rules are known to exhibit poor convergence, especially when the difference between the angle of internal friction and the dilatancy angle becomes bigger. This has often been attributed to the non-symmetry of the tangential stiffness matrix and the ensuing possible ill-conditioning. However, the computations herein suggest, and this has come out strongly in recent large-scale computations where viscoplasticity was used as regularisation method in non-associated plasticity [37], that it is actually the loss of well-posedness of the initial value problem which causes the convergence issues in the iterative solver for the non-linear problem, rather than the non-symmetry of the tangential stiffness matrix. The use of a regularisation method in non-associated plasticity therefore not only improves the mesh sensitivity, but is also hugely beneficial for computability.

Evidently, the two issues are related. Indeed, strains are now no longer localised in a single element, but are distributed over a finite width. Increasing the resolution therefore does not lead to an increase of the strains locally, which can cause serious numerical issues. Examples are local snap-backs in the elasto-plastic return mapping procedure and the occurrence of multiple, non-physical equilibrium states, which can cause divergence of the global equilibrium-finding iterative procedure.

5.2 Future work

There still exist some areas for future exploration as continuation of this work. The results of this thesis can be directly used in a wider context for the simulation of the crack propagation in pressure sensitive geomaterials while taking the off-fault plastic energy dissipation into account. It is expected that at the crack tips, there will be plastic strain localisation and therefore the developed Cosserat plasticity model will be beneficial in terms of removing any mesh size and orientation dependencies and will also improve the convergence behavior of the non-linear incremental-iterative solver.

It will also be interesting to conduct some research into the possibility of capturing the grain size effect on the orientation of shear bands using the Cosserat plasticity model in numerical simulations. Iwashita and Oda have shown in [46] that the angle of the shear band in biaxial tests varies from the Mohr-Coulomb angle to Roscoe angle as the grain size gets coarser. Investigations have already been done in the literature showing that the width of the

shear band can be determined by the characteristic length scale in the Cosserat continuum model. However, it still remains an open question whether the observed experimental dependency of the shear band angle on the grain size in granular materials can be also be captured by the characteristic length scale.

Another area where the developed Cosserat plasticity model for non-associated flow could be advantageous, is the probabilistic simulation of geotechnical problems. In order to investigate how the spatial variability of the friction and dilation angles influences the behaviour of geomaterials in localisation problems, they can be taken as random variables. Using classical plasticity models, it will not be feasible to carry out a comprehensive study with different values for friction and dilation angles due to the problems with convergence and the mesh dependencies. With the developed Cosserat plasticity model in this thesis which can be used to solve the problems caused by the non-associated plastic flow, the framework to treat these angles as independent random fields is now available. It is expected that the simulations can be done with an improved convergence behaviour showing no mesh dependency. Therefore, such a probabilistic study will become feasible and its results will be reliable.

Bibliography

[1] Ahrens, J., Geveci, B., and Law, C. (2005). Paraview: An end-user tool for large data visualization. *Visualization handbook*, 717.

[2] Altenbach, H. and Eremeyev, V. A. (2013). Cosserat media. In *Generalized Continua – From the Theory to Engineering Applications*, pages 65–130. Springer-Verlag.

[3] Andrews, D. (1976). Rupture propagation with finite stress in antiplane strain. *Journal of Geophysical Research*, 81(20):3575–3582.

[4] Andrews, D. (2005). Rupture dynamics with energy loss outside the slip zone. *Journal of Geophysical Research: Solid Earth*, 110(B1).

[5] Arthur, J., Dunstan, T., Al-Ani, Q., and Assadi, A. (1977). Plastic deformation and failure in granular media. *Géotechnique*, 27(1):53–74.

[6] Arthur, J. R. F. and Dunstan, T. (1982). Rupture layers in granular media. In *IUTAM Symp. Deformation and Failure of Granular Materials, Delft*.

[7] Bardet, J.-P. (1990). A comprehensive review of strain localization in elastoplastic soils. *Computers and geotechnics*, 10(3):163–188.

[8] Bardet, J.-P. (1991). Orientation of shear bands in frictional soils. *Journal of engineering mechanics*, 117(7):1466–1485.

[9] Bazant, Z. P., Belytschko, T. B., Chang, T.-P., et al. (1984). Continuum theory for strain-softening. *Journal of Engineering Mechanics*, 110(12):1666–1692.

[10] Bazant, Z. P. and Pijaudier-Cabot, G. (1988). Nonlocal continuum damage, localization instability and convergence. *Journal of applied mechanics*, 55(2):287–293.

[11] Bigoni, D. (2012). *Nonlinear solid mechanics: bifurcation theory and material instability*. Cambridge University Press.

[12] Bigoni, D. and Hueckel, T. (1990). A note on strain localization for a class of non-associative plasticity rules. *Ingenieur-Archiv*, 60(8):491–499.

[13] Bigoni, D. and Hueckel, T. (1991). Uniqueness and localization—i. associative and non-associative elastoplasticity. *International Journal of Solids and structures*, 28(2):197–213.

[14] Carter, J., Poon, M., and Airey, D. (2005). Numerical and semi-analytical techniques for footings subjected to combined loading. *Proceedings of IACMAG*, 11:163–76.

[15] Chang, Y. W. and Asaro, R. J. (1981). An experimental study of shear localization in aluminum-copper single crystals. *Acta Metallurgica*, 29(1):241–257.

[16] Clausen, J. (2007). *Efficient non-linear finite element implementation of elasto-plasticity for geotechnical problems*. PhD thesis.

[17] Clausen, J. and Krabbenhoft, K. (2008). Existence and uniqueness of solutions in nonassociated mohr-coulomb elastoplasticity. In *Proc. WCCM VIII, Venice*.

[18] Coombs, W. M., Crouch, R. S., and Heaney, C. E. (2013). Observations on mohr-coulomb plasticity under plane strain. *Journal of Engineering Mechanics*, 139(9):1218–1228.

[19] Cosserat, E. and Cosserat, F. (1909). *Théorie des Corps Déformables*. A. Hermann et fils, Paris.

[20] Costin, L., Crisman, E., Hawley, R. H., and Duffy, J. (1980). On the localisation of plastic flow in mild steel tubes under dynamic torsional loading. In *Proc. 2 nd Conf. Mechanical Properties of Materials at High Rates of Strain, Oxford, England, Mar. 1979,*, pages 90–100.

[21] Coulomb, C. (1776). Essai sur une application des règles des maximis et minimis à quelques problèmes de statique. *Memoires Acad. Royale des Sciences*, 7:343–382.

[22] Cox, T. and Low, J. R. (1974). An investigation of the plastic fracture of aisi 4340 and 18 nickel-200 grade maraging steels. *Metallurgical Transactions*, 5(6):1457–1470.

[23] de Borst, R. (1986). *Non-linear analysis of frictional materials*. PhD thesis, Delft University of Technology, Delft, The Netherlands.

[24] de Borst, R. (1988). Bifurcations in finite element models with a non-associated flow law. *International Journal for Numerical and Analytical Methods in Geomechanics*, 12:99–116.

[25] de Borst, R. (1991). Simulation of strain localization: A reappraisal of the Cosserat continuum. *Engineering Computations*, 8:317–332.

[26] de Borst, R. (1993). A generalisation of J2-flow theory for polar continua. *Computer Methods in Applied Mechanics and Engineering*, 103:347–362.

[27] de Borst, R. (2013). Computational methods for generalised continua. In *Generalized Continua from the Theory to Engineering Applications*, pages 361–388. Springer.

[28] de Borst, R., Crisfield, M. A., Remmers, J. J., and Verhoosel, C. V. (2012). *Nonlinear finite element analysis of solids and structures*. John Wiley & Sons.

[29] de Borst, R. and Mühlhaus, H.-B. (1992). Gradient-dependent plasticity: formulation and algorithmic aspects. *International Journal for Numerical Methods in Engineering*, 35(3):521–539.

[30] de Borst, R. and Sluys, L. J. (1991). Localisation in a Cosserat continuum under static and dynamic loading conditions. *Computer Methods in Applied Mechanics and Engineering*, 90:805–827.

[31] de Borst, R., Sluys, L. J., Mühlhaus, H.-B., and Pamin, J. (1993). Fundamental issues in finite element analysis of localisation of deformation. *Engineering Computations*, 10:99–122.

[32] de Souza Neto, E. A., Peric, D., and Owen, D. R. (2011). *Computational methods for plasticity: theory and applications*. John Wiley & Sons.

[33] Desrues, J. (1984). *La localisation de la déformation dans les matériaux granulaires*. PhD thesis, Institut National Polytechnique de Grenoble.

[34] Dietsche, A., Steinmann, P., and Willam, K. (1993). Micropolar elastoplasticity and its role in localization. *International Journal of Plasticity*, 9(7):813–831.

[35] Drucker, D. C. and Prager, W. (1952). Soil mechanics and plastic analysis or limit design. *Quarterly of applied mathematics*, 10(2):157–165.

[36] Dunne, F. and Petrinic, N. (2005). *Introduction to computational plasticity*. Oxford University Press.

[37] Duretz, T., de Borst, R., and Le Pourhiet, L. (2019). On finite thickness of shear bands in frictional viscoplasticity, and implications for lithosphere dynamics. *Geochemistry, Geophysics, Geosystems*, (submitted).

[38] Duthilleul, B. (1983). *Rupture progressive: simulation physique et numérique*. PhD thesis, Institut National Polytechnique de Grenoble.

[39] Dynaflow Research Group (2016). Jive v2.2. http://www.jem-jive.com.

[40] Ehlers, W. and Scholz, B. (2007). An inverse algorithm for the identification and the sensitivity analysis of the parameters governing micropolar elasto-plastic granular material. *Archive of Applied Mechanics*, 77:911–931.

[41] Hadamard, J. (1903). *Leçons sur la propagation des ondes et les équations de l'hydrodynamique*. A. Hermann.

[42] Hansen, B. (1958). Line ruptures regarded as narrow rupture zones-basic equations based on kinematic considerations. In *Proc., Conf. on Earth Pressure Problems*, volume 1, pages 39–48.

[43] Hill, R. (1958). A general theory of uniqueness and stability in elastic-plastic solids. *Journal of the Mechanics and Physics of Solids*, 6:236–249.

[44] Hill, R. (1962). Acceleration waves in solid. *Journal of the Mechanics and Physics of Solids*, 10:1–16.

[45] Hill, R. (1998). *The mathematical theory of plasticity*, volume 11. Oxford university press.

[46] Iwashita, K. and Oda, M. (1999). *Mechanics of granular materials: an introduction*. CRC press.

[47] Koiter, W. T. (1953). Stress-strain relations, uniqueness and variational theorems for elastic-plastic materials with a singular yield surface. *Quarterly of applied mathematics*, 11(3):350–354.

[48] Krabbenhoft, K., Karim, M., Lyamin, A., and Sloan, S. (2012). Associated computational plasticity schemes for nonassociated frictional materials. *International Journal for Numerical Methods in Engineering*, 90(9):1089–1117.

[49] Lakes, R. (2016). Physical meaning of elastic constants in cosserat, void, and microstretch elasticity. *Journal of Mechanics of Materials and Structures*, 11(3):217–229.

[50] Le Pourhiet, L. (2013). Strain localization due to structural softening during pressure sensitive rate independent yielding. *Bulletin de la Société géologique de France*, 184:357–371.

[51] Loret, B. and Prevost, J. H. (1990). Dynamic strain localization in elasto-(visco-) plastic solids, part 1. general formulation and one-dimensional examples. *Computer Methods in Applied Mechanics and Engineering*, 83(3):247–273.

[52] Loukidis, D. and Salgado, R. (2009). Bearing capacity of strip and circular footings in sand using finite elements. *Computers and Geotechnics*, 36(5):871–879.

[53] Mandel, J. (1966). Conditions de stabilité et postulat de Drucker. In *Proceedings IUTAM Symposium on Rheology and Soil Mechanics*, pages 58–68, Berlin. Springer-Verlag.

[54] Manzari, M. T. and Nour, M. A. (2000). Significance of soil dilatancy in slope stability analysis. *Journal of Geotechnical and Geoenvironmental Engineering*, 126(1):75–80.

[55] MathWorks (2012). Matlab and statistics toolbox release 2012b.

[56] Mazière, M. and Forest, S. (2015). Strain gradient plasticity modeling and finite element simulation of Lüders band formation and propagation. *Continuum Mechanics and Thermodynamics*, 27:83–104.

[57] Melan, E. (1938). Zur plastizität des räumlichen kontinuums. *Archive of Applied Mechanics*, 9(2):116–126.

[58] Mühlhaus, H. and Vardoulakis, I. (1987). The thickness of shear bands in granular materials. *Géotechnique*, 37(3):271–283.

[59] Mises, R. v. (1928). Mechanik der plastischen formänderung von kristallen. *ZAMM-Journal of Applied Mathematics and Mechanics/Zeitschrift für Angewandte Mathematik und Mechanik*, 8(3):161–185.

[60] Mühlhaus, H. (1988). Lamination phenomena in prestressed rock. In *2nd Int. Symp. on Rockbursts and Seismicity in Mines*, pages 117–128. Univ. of Minnesota Minneapolis.

[61] Mühlhaus, H.-B. (1989). Application of cosserat theory in numerical solutions of limit load problems. *Ingenieur-Archiv*, 59(2):124–137.

[62] Mühlhaus, H.-B. and Alfantis, E. (1991). A variational principle for gradient plasticity. *International Journal of Solids and Structures*, 28(7):845–857.

[63] Mühlhaus, H. B. and Vardoulakis, I. (1987). The thickness of shear bands in granular materials. *Géotechnique*, 37:271–283.

[64] Naghdi, P. (1960). Stress-strain relations in plasticity and thermoplasticity. In *Plasticity: Proceedings of the Second Symposium on Naval Structural Mechanics*, pages 121–169. Pergamon.

[65] Needleman, A. (1979). Non-normality and bifurcation in plane strain tension and compression. *Journal of the Mechanics and Physics of Solids*, 27:231–254.

[66] Needleman, A. (1988). Material rate dependence and mesh sensitivity in localization problems. *Computer methods in applied mechanics and engineering*, 67(1):69–85.

[67] Ortiz, M. and Popov, E. P. (1985). Accuracy and stability of integration algorithms for elastoplastic constitutive relations. *International journal for numerical methods in engineering*, 21(9):1561–1576.

[68] Pamin, J., Askes, H., and de Borst, R. (2003). Two gradient plasticity theories discretized with the element-free Galerkin method. *Computer Methods in Applied Mechanics and Engineering*, 192:2377–2407.

[69] Papanastasiou, P. and Zervos, A. (2004). Wellbore stability analysis: from linear elasticity to postbifurcation modeling. *International Journal of Geomechanics*, 4(1):2–12.

[70] Papanastasiou, P. C. and Vardoulakis, I. G. (1992). Numerical treatment of progressive localization in relation to borehole stability. *International Journal for Numerical and Analytical Methods in Geomechanics*, 16(6):389–424.

[71] Peerlings, R. H., de Borst, R., Brekelmans, W. M., and De Vree, J. (1996). Gradient enhanced damage for quasi-brittle materials. *International Journal for numerical methods in engineering*, 39(19):3391–3403.

[72] Pijaudier-Cabot, G. and Bažant, Z. P. (1987). Nonlocal damage theory. *Journal of engineering mechanics*, 113(10):1512–1533.

[73] Poliakov, A. N., Dmowska, R., and Rice, J. R. (2002). Dynamic shear rupture interactions with fault bends and off-axis secondary faulting. *Journal of Geophysical Research: Solid Earth*, 107(B11):ESE–6.

[74] Prager, W. (1955). The theory of plasticity: a survey of recent achievements. *Proceedings of the Institution of Mechanical Engineers*, 169(1):41–57.

[75] Prandtl, L. (1920). Über die härte plastischer körper. *Nachrichten von der Gesellschaft der Wissenschaften zu Göttingen, Mathematisch-Physikalische Klasse*, 1920:74–85.

[76] Read, H. E. and Hegemier, G. A. (1984). Strain softening of rock, soil and concrete – a review article. *Mechanics of Materials*, 3:271–294.

[77] Reynolds, O. (1885). On the dilatancy of media composed of rigid particles in contact with experimental observations. *Philosophical Magazine (Series 5)*, 20:469–481.

[78] Rice, J. (1979). *The mechanics of earthquake rupture*. Division of Engineering, Brown University Providence.

[79] Rice, J. and Rudnicki, J. (1980). A note on some features of the theory of localization of deformation. *International Journal of solids and structures*, 16(7):597–605.

[80] Rice, J. R. (1976). The localization of plastic deformation. *Theoretical and Applied Mechanics (Proceedings of the 14th International Congress on Theoretical and Applied Mechanics)*, 1:207–220.

[81] Rice, J. R., Sammis, C. G., and Parsons, R. (2005). Off-fault secondary failure induced by a dynamic slip pulse. *Bulletin of the Seismological Society of America*, 95(1):109–134.

[82] Rodríguez-Ferran, A., Bennett, T., Askes, H., and Tamayo-Mas, E. (2011). A general framework for softening regularisation based on gradient elasticity. *International Journal of Solids and Structures*, 48(9):1382–1394.

[83] Roscoe, K. H. (1970). The influence of strains in soil mechanics. *Géotechnique*, 20(2):129–170.

[84] Rudnicki, J. W. and Rice, J. R. (1975). Conditions for the localization of deformation in pressure sensitive dilatant materials. *Journal of the Mechanics and Physics of Solids*, 23:371–394.

[85] Sabet, S. A. and de Borst, R. (2017). A finite element model for fault rupture. In *Proceedings of the 25th UKACM Conference on Computational Mechanics*, pages 142–145. University of Birmingham.

[86] Sabet, S. A. and de Borst, R. (2019a). A cosserat continuum approach to non-associated plasticity. In *The 5th ECCOMAS Young Investigators Conference*, pages 29–30. AGH University of Science and Technology, Kraków, Poland.

[87] Sabet, S. A. and de Borst, R. (2019b). Mesh bias and shear band inclination in standard and non-standard continua. *Archive of Applied Mechanics*, 89(12):2577–2590.

[88] Sabet, S. A. and de Borst, R. (2019c). Structural softening, mesh dependence, and regularisation in non-associated plastic flow. *International Journal for Numerical and Analytical Methods in Geomechanics*, 43(13):2170–2183.

[89] Scarpelli, G. and Wood, D. M. (1982). Experimental observations of shear patterns in direct shear tests. In *IUTAM Deformation and Failure of Granular Materials Conference, Delft*, pages 473–483.

[90] Schaefer, H. (1962). Versuch einer elastizitätstheorie des zweidimensionalen ebenen cosserat-kontinuum. *Miszellaneen der angewandte Mechanik*, pages 277–292.

[91] Schaefer, H. (1967). Das Cosserat-Kontinuum. *Zeitschrief für Angewandte Mathematik und Mechanik*, 47:485–498.

[92] Schellekens, J. and De Borst, R. (1993). On the numerical integration of interface elements. *International Journal for Numerical Methods in Engineering*, 36(1):43–66.

[93] Simo, J. C. and Hughes, T. J. (2006). *Computational inelasticity*, volume 7. Springer Science & Business Media.

[94] Simo, J. C. and Taylor, R. L. (1985). Consistent tangent operators for rate-independent elastoplasticity. *Computer methods in applied mechanics and engineering*, 48(1):101–118.

[95] Sloan, S. W., Abbo, A. J., and Sheng, D. (2001). Refined explicit integration of elastoplastic models with automatic error control. *Engineering Computations*.

[96] Sluys, L. J. (1992). *Wave Propagation, Localisation and Dispersion in Softening Solids*. PhD thesis, TU Delft, Delft.

[97] Sulem, J. and Vardoulakis, I. (1995). *Bifurcation analysis in geomechanics*. CRC Press.

[98] Tejchman, J. and Bauer, E. (1996). Numerical simulation of shear band formation with a polar hypoplastic constitutive model. *Computers and Geotechnics*, 19(3):221–244.

[99] Templeton, E. L. and Rice, J. R. (2008). Off-fault plasticity and earthquake rupture dynamics: 1. dry materials or neglect of fluid pressure changes. *Journal of Geophysical Research: Solid Earth*, 113(B9).

[100] Thomas, T. Y. (1961). *Plastic Flow and Fracture in Solids*, volume 2. Elsevier.

[101] Triantafyllidis, N. and Aifantis, E. C. (1986). A gradient approach to localization of deformation. i. hyperelastic materials. *Journal of Elasticity*, 16(3):225–237.

[102] Van Mier, J. G. M. (1984). *Strain-softening of concrete under multiaxial loading conditions*. PhD thesis, Technische Hogeschool Eindhoven.

[103] Vardoulakis, I. (1979). Bifurcation analysis of the triaxial test on sand samples. *Acta Mechanica*, 32(1-3):35–54.

[104] Vardoulakis, I. (1980). Shear band inclination and shear modulus of sand in biaxial tests. *International Journal for Numerical and Analytical Methods in Geomechanics*, 4:103–119.

[105] Vardoulakis, I. (1983). Rigid granular plasticity model and bifurcation in the triaxial test. *Acta Mechanica*, 49(1-2):57–79.

[106] Vardoulakis, I. (2018). *Cosserat Continuum Mechanics: With Applications to Granular Media*, volume 87. Springer.

[107] Vermeer, P. (1982). A simple shear-band analysis using compliances. In *Proc. of the IUTAM Conf. on Deformation and Failure of Granular Materials*, pages 493–499.

[108] Vermeer, P. A. (1990). The orientation of shear bands in biaxial tests. *Géotechnique*, 40:223–234.

[109] Vermeer, P. A. and de Borst, R. (1984). Non-associated plasticity for soils, concrete and rock. *HERON, 29 (3)*.

[110] Viesca, R. C., Templeton, E. L., and Rice, J. R. (2008). Off-fault plasticity and earthquake rupture dynamics: 2. effects of fluid saturation. *Journal of Geophysical Research: Solid Earth*, 113(B9).

[111] Vignollet, J., May, S., and de Borst, R. (2015). On the numerical integration of isogeometric interface elements. *International Journal for Numerical Methods in Engineering*, 102(11):1733–1749.

[112] Vignollet, J., May, S., and de Borst, R. (2016). Isogeometric analysis of fluid-saturated porous media including flow in the cracks. *International Journal for Numerical Methods in Engineering*, 108(9):990–1006.

[113] Wang, W. M., Sluys, L. J., and de Borst, R. (1997). Viscoplasticity for instabilities due to strain softening and strain-rate softening. *International Journal for Numerical Methods in Engineering*, 40:3839–3864.

[114] Wawersik, W. and Brace, W. (1971). Post-failure behavior of a granite and diabase. *Rock mechanics*, 3(2):61–85.

[115] Wawersik, W. and Fairhurst, C. (1970). A study of brittle rock fracture in laboratory compression experiments. In *International Journal of Rock Mechanics and Mining Sciences & Geomechanics Abstracts*, volume 7, pages 561–575. Elsevier.

[116] Zervos, A., Papanastasiou, P., and Vardoulakis, I. (2001). A finite element displacement formulation for gradient elastoplasticity. *International Journal for Numerical Methods in Engineering*, 50(6):1369–1388.

[117] Zervos, A., Vardoulakis, I., Jean, M., and Lerat, P. (2000). Numerical investigation of granular interfaces kinematics. *Mechanics of Cohesive-frictional Materials: An International Journal on Experiments, Modelling and Computation of Materials and Structures*, 5(4):305–324.